Polarized vector boson scattering in the fully leptonic WZ and ZZ channels at the LHC

A. Ballestrero,[a] **E. Maina**[a,b] **and G. Pelliccioli**[a,b]

[a]*INFN, Sezione di Torino,*
  Via P. Giuria 1, I-10125 Torino, Italy

[b]*Dipartimento di Fisica, Università di Torino,*
  Via P. Giuria 1, I-10125 Torino, Italy

 E-mail: ballestr@to.infn.it, maina@to.infn.it, gpellicc@to.infn.it

ABSTRACT: Isolating the scattering of longitudinal weak bosons at the LHC is an important tool to probe the ElectroWeak Symmetry Breaking mechanism. Separating polarizations of W and Z bosons is complicated, because of non resonant contributions and interference effects. Additional care is necessary when considering Z bosons, due to the γ/Z mixing in the coupling to charged leptons.

We propose a method to define polarized signals in ZZ and W^+Z scattering at the LHC, which relies on the separation of weak boson polarizations at the amplitude level in Monte Carlo simulations.

After validation in the absence of lepton cuts, we investigate how polarized distributions are affected by a realistic set of kinematic cuts (and neutrino reconstruction, when needed). The total and differential polarized cross sections computed at the amplitude level are well defined, and their sum reproduces the full results, up to non negligible but computable interference effects which should be included in experimental analyses. We show that polarized cross sections computed using the reweighting method are inaccurate, particularly at large energies. We also present two procedures which address the model independent extraction of polarized components from LHC data, using Standard Model angular distribution templates.

KEYWORDS: Beyond Standard Model, Higgs Physics

Contents

1 Introduction

Vector Boson Scattering (VBS) of longitudinally polarized, on shell, W's and Z's is the perfect exemplification of the interplay of gauge invariance and unitarity in ElectroWeak Symmetry Breaking (EWSB). The delicate cancellations which occur in the set of diagrams which involve only the exchange of vector bosons and between them and the Higgs exchange diagrams are crucial for Unitarity. These cancellations are not needed when the scattering involves transverse polarized vector bosons. Hence a polarization analysis of VBS nicely complements the study of Higgs boson properties in the effort to fully characterize the details of the EWSB mechanism.

Since vector boson lifetimes are too short to allow for stable beams or direct observation before decay, we can only access VBS as a subprocess of more complicated reactions which include the emission of weak bosons from initial state quarks and their decay to stable particles.

In Run 2 CMS and ATLAS have finally produced convincing evidence that VBS actually takes place in the complex environment of the LHC [1–5]. Unfortunately, the statistics is still too small for any attempt to analyze vector boson polarizations. Hopefully the higher rates which will be available after the Long Stop in 2019 and 2020 and later in the High Luminosity phase of the LHC will allow polarization studies [6, 7].

Vector boson polarizations at the LHC have been studied in a number of papers. $W+$ jets processes, without cuts on the charged leptons, have been studied in ref. [8]. The modifications introduced by selection cuts have been examined in ref. [9], where, in addition to $W+$ jets, several other W and Z production mechanisms have been discussed. The interplay between interference among polarizations and selection cuts has also been analyzed in ref. [10]. Recently, the vector boson polarizations in $pp \to WZ$ have been studied, taking into account both QCD and EW NLO corrections [11].

Both CMS and ATLAS have measured the W polarization fractions in the $W+$ jets [12, 13] channel and in $t\bar{t}$ events [14, 15].

In the Feynman amplitudes which describe VBS in a realistic accelerator framework, all information about the vector boson polarization is confined to the polarization sum in the corresponding propagators. Therefore, the individual polarizations interfere among themselves. These interference contributions cancel exactly only when an integration over the full azimuth of the decay products is performed. Acceptance cuts, however, inhibit collecting data over the full angular range and the cancellation cannot be complete.

In addition, electroweak boson production processes are typically described by amplitudes including non resonant diagrams, which cannot be interpreted as production times decay of any vector boson. These diagrams are essential for gauge invariance and cannot be ignored. For them, separating polarizations is simply unfeasible.

In a previous paper [16], we have shown that it is possible to define, in a simple and natural way, cross sections corresponding to vector bosons of definite polarization.

We have further demonstrated that the sum of cross sections with definite polarization, even in the presence of cuts on the final state leptons, describes reasonably well the full total cross section and most of the differential distributions. Therefore, it is possible to fit the data using single polarized templates and the interference, to extract polarization fractions.

In ref. [16] we have focused on the jjW^+W^- final state, with both W's decaying leptonically, as a proof of concept of our method to separate the different polarizations, without worrying too much about its practical observability.

In this paper we study $jj\,e^+e^-\mu^+\mu^-$ and $jj\,\mu^+\nu_\mu e^+e^-$. The cross section for the first reaction is small, but the decay angles for each Z and the invariant mass of the ZZ pair can be determined with high precision. The WZ channel has a much larger cross section but, as any reaction involving a W decaying leptonically, is affected by the need to reconstruct the unknown component along the beam direction of the neutrino momentum.

This reconstruction, from which the decay distribution of the W and the total mass of the WZ system are inferred, can only be approximate.

In section 2 we recall the basic features of unstable vector boson polarizations and their relationship with the angular distribution of the charged fermions produced in the boson decay. In section 3 we present our proposal for a definition of polarized amplitudes which entails dropping non resonant diagrams and projecting the resulting amplitude on the vector boson mass shell. In sections 4 and 5 we study the production of ZZ and WZ pairs in VBS, first in the absence of cuts on the leptonic variables and then in the realistic case in which acceptance cuts are imposed. In both cases we focus on how well the sum of single polarized cross sections reproduces the full result. In section 6 we compare our approach to the reweighting procedure which has been so far adopted in experimental analyses. In section 7 we discuss, using the $M_h \to \infty$ toy model, to what extent the angular distribution obtained, in the presence of lepton cuts, in the SM can be employed for extracting polarization fractions from the data even in case the underlying dynamics goes beyond the Standard Model. Finally, in section 8 we summarize our findings.

2 Vector bosons polarization and angular distributions of their decay products

Let us consider an amplitude in which a weak vector boson decays to a final state fermion pair. In the Unitary Gauge, it can be expressed as

$$\mathcal{M} = \mathcal{M}_\mu \frac{i}{k^2 - M^2 + i\Gamma M} \left(-g^{\mu\nu} + \frac{k^\mu k^\nu}{M^2} \right) \left[-i\,g\,\bar{\psi}_f\,\gamma_\nu \left(c_L \frac{1-\gamma^5}{2} + c_R \frac{1+\gamma^5}{2} \right) \psi_{f'} \right], \quad (2.1)$$

where M and Γ are the vector boson mass and width, respectively. c_R and c_L are the right and left handed couplings of the fermions to the $W^+(Z)$, as shown in table 1.

The polarization tensor can be expressed in terms of four polarization vectors [17]

$$-g^{\mu\nu} + \frac{k^\mu k^\nu}{M^2} = \sum_{\lambda=1}^{4} \varepsilon_\lambda^\mu(k) \varepsilon_\lambda^{\nu*}(k). \quad (2.2)$$

In the following we call single polarized amplitude with polarization λ an amplitude in which the sum on the left hand side of eq. (2.2) is substituted by one of the terms on the right hand side, $\sum_{\lambda'} \varepsilon_{\lambda'}^\mu \varepsilon_{\lambda'}^{\nu*} \to \varepsilon_\lambda^\mu \varepsilon_\lambda^{\nu*}$.

In a frame in which the off shell vector boson propagates along the (θ_V, ϕ_V) axis, with three momentum κ, energy E and invariant mass $\sqrt{Q^2} = \sqrt{E^2 - \kappa^2}$, the polarizations vectors read:

$$\varepsilon_L^\mu = \frac{1}{\sqrt{2}}(0, \cos\theta_V \cos\phi_V + i\sin\phi_V, \cos\theta_V \sin\phi_V - i\cos\phi_V, -\sin\theta_V) \text{ (left)},$$

$$\varepsilon_R^\mu = \frac{1}{\sqrt{2}}(0, -\cos\theta_V \cos\phi_V + i\sin\phi_V, -\cos\theta_V \sin\phi_V - i\cos\phi_V, \sin\theta_V) \text{ (right)}, \quad (2.3)$$

$$\varepsilon_0^\mu = (\kappa, E\sin\theta_V \cos\phi_V, E\sin\theta_V \sin\phi, E\cos\theta_V)/\sqrt{Q^2} \text{ (longitudinal)},$$

$$\varepsilon_A^\mu = \sqrt{\frac{Q^2 - M^2}{Q^2 M^2}}(E, \kappa\sin\theta_V \cos\phi_V, \kappa\sin\theta_V \sin\phi_V, \kappa\cos\theta_V) \text{ (auxiliary)}.$$

In this paper, they are computed in the lab frame.

	c_L	c_R
W	$1/(s\sqrt{2})$	0
Z	$(I^3_{W,f} - s^2 Q_f)/(s\,c)$	$-s\,Q_f/c$

Table 1. Weak couplings. $c = \cos\theta_W = M_W/M_Z$, $s = \sin\theta_W$.

The auxiliary polarization in eq. (2.2) does not contribute if the decay fermions are massless. Therefore, the normalized cross section, after integration over the azimuthal angle of the decay products, can be expressed, in the absence of cuts on decay leptons, as follows:

$$\frac{1}{\frac{d\sigma(X)}{dX}} \frac{d\sigma(\theta,X)}{d\cos\theta\,dX} = \frac{3}{8} f_L(X)\left(1+\cos^2\theta - \frac{2(c_L^2 - c_R^2)}{(c_L^2 + c_R^2)}\cos\theta\right)$$
$$+ \frac{3}{8} f_R(X)\left(1+\cos^2\theta + \frac{2(c_L^2 - c_R^2)}{(c_L^2 - c_R^2)}\cos\theta\right) + \frac{3}{4} f_0(X)\sin^2\theta, \quad (2.4)$$

X stands for all additional phase space variables in addition to the decay angle θ. The three polarization fractions f_L, f_0, f_R sum to one. For W^+ leptonic decays, θ is the angle measured in the W^+ rest frame between the charged particle and the W^+ direction of flight in the lab frame. For Z decays, θ is the angle measured in the Z rest frame between the antifermion and the Z direction of flight in the lab frame. For W^-, $\cos\theta \to -\cos\theta$.

Hence, each physical polarization is uniquely associated with a specific angular distribution of the charged lepton, even when the vector boson is off mass shell.

Defining polarized production and decay amplitudes,

$$\mathcal{M}^{\mathcal{P}}{}_\lambda = \mathcal{M}_\mu \varepsilon^\mu_\lambda, \qquad \mathcal{M}^{\mathcal{D}}{}_\lambda = \varepsilon^{\nu*}_\lambda(k)\left[-i\,g\,\bar{\psi}_f\,\gamma_\nu\left(c_L\frac{1-\gamma^5}{2} + c_R\frac{1+\gamma^5}{2}\right)\psi_{f'}\right], \quad (2.5)$$

the full amplitude can be written as:

$$\mathcal{M} = \sum_{\lambda=1}^{3} \mathcal{M}^{\mathcal{P}}{}_\lambda \frac{i}{k^2 - M^2 + i\Gamma M} \mathcal{M}^{\mathcal{D}}{}_\lambda = \sum_{\lambda=1}^{3} \mathcal{M}^{\mathcal{F}}{}_\lambda, \quad (2.6)$$

where $\mathcal{M}^{\mathcal{F}}{}_\lambda$ is the amplitude with a single polarization for the intermediate vector boson. Notice that in each $\mathcal{M}^{\mathcal{F}}{}_\lambda$ all correlations between production and decay are exact.

The squared amplitude becomes:

$$\underbrace{|\mathcal{M}|^2}_{\text{coherent sum}} = \underbrace{\sum_\lambda |\mathcal{M}^{\mathcal{F}}{}_\lambda|^2}_{\text{incoherent sum}} + \underbrace{\sum_{\lambda\neq\lambda'} \mathcal{M}^{\mathcal{F}*}{}_\lambda \mathcal{M}^{\mathcal{F}}{}_{\lambda'}}_{\text{interference terms}}. \quad (2.7)$$

The interference terms in eq. (2.7) are not, in general, zero. They cancel only when the squared amplitude is integrated over the full range of the angle ϕ. Acceptance cuts on the charged leptons and on the transverse missing momentum, unavoidable in practice, prevent from full ϕ integration. They break the factorization of the angular dependence of the decay from that on the remaining kinematic variables X which is embodied in eq. (2.4).
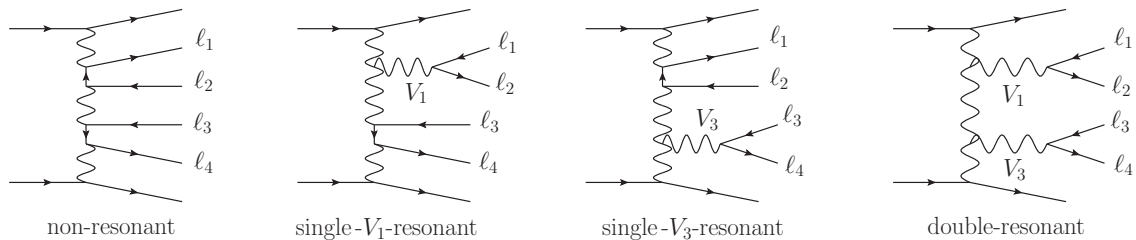
Figure 1. Sample tree level diagrams for VBS at the LHC. Scattering diagrams (like the rightmost one) are only a subset of double resonant diagrams.

Cuts affect differently the different single polarized angular decay distributions. The effect depends on the kinematics of the intermediate vector bosons which in turn is determined by the underlying physics model.

We now turn to VBS processes which feature two lepton pairs in the final state produced in association with two quarks. Here and in all the following we consider pure electroweak contributions at tree level, $\mathcal{O}(\alpha^6)$. Let us assume for simplicity that the final state lepton flavours are chosen such that ℓ_1, ℓ_2 can be decay products of a vector boson V_1 and ℓ_3, ℓ_4 can be decay products of a boson V_3. In such a situation, non resonant diagrams, single-V_1-resonant, single-V_3-resonant and double resonant diagrams contribute to the tree level amplitude. Sample diagrams are shown in figure 1. In order to separate the polarizations of V_1, non resonant and single-V_3-resonant contributions must be dropped. Analogously, non resonant and single-V_1-resonant contributions must be dropped to separate V_3 polarizations. Dropping a set of diagrams may violate gauge invariance. If this results in large numerical discrepancies we need a procedure to produce a reliable prediction. If both V_1 and V_3 are W bosons, we have shown [16] that the selection of double resonant diagrams can give physical predictions (i.e. approximate the full computation), provided that double On Shell projections (OSP) are performed on the two W's. Such procedure is known in the literature as Double Pole Approximation [18–22], and preserves the gauge invariance of squared electroweak amplitudes that can be written as the production of two massive vector bosons times their leptonic decay. In the WW final state, an additional advantage of this method consists in avoiding any invariant mass cut on decay products of W bosons (lepton-neutrino pairs) to reproduce accurately the results of the full calculation.

The pole approximation has an intrinsic uncertainty of Γ/M and thus of a few percent for weak bosons. Since polarizations of intermediate unstable particles have no sound theoretical basis and their definition necessarily depends on conventions and approximations, predictions beyond this accuracy should not, in any case, be expected.

3 Separating Z resonant contributions

As an introduction to separating polarizations in processes with Z bosons which decay leptonically, we briefly recall the main issues which affect isolating polarizations in the WW channel in VBS [16]. In table 2 we show cross sections for two partonic channels con-

$\mathbf{\Delta_M}$	**FULL**	**RES OSP**	**RES NO OSP**
$u\ u \to u\ u\ e^-\ \bar{\nu}_e\ \mu^+\ \nu_\mu$ (2Z2W)			
∞ (no cut)	403.3 (4)	398.1(4)	1025.9(9)
$u\ s \to d\ c\ e^-\ \bar{\nu}_e\ \mu^+\ \nu_\mu$ (4W)			
∞ (no cut)	23.80(3)	23.62(2)	29.11(4)

Table 2. Cross sections in attobarns (ab) for some VBS processes, for $|M_{\ell\nu_\ell} - M_W| < \Delta_M$ $(\ell = e, \mu)$. All diagrams are taken into account for the full calculation (FULL), while only double resonant diagrams contribute to the two rightmost columns, with (RES OSP) and without (RES NO OSP) projection. Selection cuts are: $p_t^j > 20\,\text{GeV}$, $|\eta_j| < 5.5$, $M_{jj} > 600\,\text{GeV}$, $|\Delta\eta_{jj}| > 3.6$, $M_{4\ell} > 300\,\text{GeV}$.
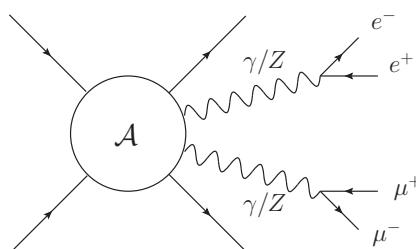

Figure 2. γ/Z resonant diagrams in $pp \to jje^+e^-\mu^+\mu^-$.

tributing to $pp \to jje^-\bar{\nu}_e\mu^+\nu_\mu$. The first process receives contributions only from 2Z2W amplitudes, i.e. it includes $ZZ \to W^+W^-$ scattering diagrams. The second process receives contributions only from 4W amplitudes, as it includes $W^+W^- \to W^+W^-$ scattering diagrams. In both cases the full result (FULL) is reproduced at the 1% level by the On Shell projected one (RES OSP). If double On Shell projections are not applied (RES NO OSP), double resonant diagrams fail to reproduce the full result, since gauge invariance is violated and no cut on $M_{\ell\nu_\ell}$ is imposed. We note that unprojected resonant diagrams overestimate the cross section much more in the 2Z2W process (+150%) than in 4W one (+25%).

3.1 *ZZ* processes

We now consider VBS ZZ production in the four charged leptons decay channel ($pp \to jj\,e^-e^+\mu^-\mu^+$), which contains both $ZZ \to ZZ$ and $W^+W^- \to ZZ$ scattering. Therefore, some VBS processes receive contributions only from 4Z amplitudes, others only from 2W2Z amplitudes. Some processes, which we label mixed, receive contributions from both of them. In the Standard Model, charged leptons couple both to the Z boson and to the photon: this issue, when studying Z bosons phenomenology, is usually treated by selecting lepton pair invariant masses close to the Z pole mass (M_Z). In VBS, $\gamma\gamma$ and γZ resonant diagrams interfere with ZZ resonant ones, as shown in figure 2.

The OSP treatment of ZZ resonant diagrams, defined in complete analogy with the one applied for WW in ref. [16], is a gauge invariant procedure, i.e. preserves SU(2) and U(1) Ward identities. However, it leads to results which are not sufficiently close to the full ones. We have computed a 4Z process contributing to ZZ VBS production, with

Δ_M	FULL	RES OSP	RES NO OSP
$u\,u \to u\,u\,e^-\,e^+\,\mu^-\,\mu^+$ (4Z)			
∞ (no cut)	0.4479(5)	0.1302(2)	0.1318(2)
30 GeV	0.1776(5)	0.1264(2)	0.1266(2)
5 GeV	0.1009(1)	0.0955(2)	0.0953(1)

Table 3. Cross sections (ab) for $u\,u \to u\,u\,e^-e^+\mu^-\mu^+$, for $|M_{\ell^+\ell^-} - M_Z| < \Delta_M$ ($\ell = e, \mu$). All diagrams are taken into account for the full calculation (FULL), while only double resonant diagrams contribute to the two rightmost columns, with (RES OSP) and without (RES NO OSP) projection. Selection cuts are: $p_t^j > 20\,\text{GeV}$, $|\eta_j| < 5.5$, $M_{jj} > 600\,\text{GeV}$, $|\Delta\eta_{jj}| > 3.6$, $M_{4\ell} > 300\,\text{GeV}$, $M_{\ell^+\ell^-} > 40$ GeV.

different cuts on $|M_{\ell^+\ell^-} - M_Z|$ of both lepton pairs, either including all diagrams, or selecting only ZZ resonant diagrams (with or without OSP). We have imposed standard cuts on single jet kinematics ($p_t^j > 20\,\text{GeV}$, $|\eta_j| < 5.5$), strong VBS cuts on the jet pair ($M_{jj} > 600\,\text{GeV}$, $|\Delta\eta_{jj}| > 3.6$), a minimum invariant mass of the four leptons system ($M_{4\ell} > 300\,\text{GeV}$), and a minimum invariant mass cut on same flavour opposite sign lepton pairs ($M_{\ell^+\ell^-} > 40$ GeV), to avoid infrared singularities due to $\gamma^* \to \ell^+\ell^-$ diagrams.

Numerical results for the total cross sections are shown in table 3. If no cut is imposed on $|M_{\ell^+\ell^-} - M_Z|$, double resonant ZZ diagrams fail badly to describe the full result (either with or without OSP): this is the effect of neglecting resonant γZ and $\gamma\gamma$ diagrams, which interfere with ZZ ones giving large contributions in the low $M_{\ell^+\ell^-}$ region, despite the $M_{\ell^+\ell^-} > 40$ GeV cut. The situation slightly improves when imposing the cut $|M_{\ell^+\ell^-} - M_Z| < 30\,\text{GeV}$, but the resonant predictions are still unreliable as they underestimate by 30% the full result. Imposing a sharper cut on $|M_{\ell^+\ell^-} - M_Z|$ (5 GeV), the ZZ resonant diagrams still underestimate by 5% the full cross section. It is evident that the discrepancy between the resonant and full calculations is due to the γ/Z mixing, not only at the level of the decay into charged leptons, but more generally at the level of the complete amplitude. In any case, the application of On Shell projections doesn't change substantially the resonant calculation.

We have investigated further this effect, by simulating the same process with final state neutrinos, instead of charged leptons, i.e. $u\,u \to u\,u\,\nu_e\bar{\nu}_e\nu_\mu\bar{\nu}_\mu$. Numerical results are shown in table 4. The presence of neutrinos implies that there are no contributions in which the photon couples to the final state leptons. In fact, the large discrepancy between full and resonant results obtained in the four charged leptons case (first line of table 3) is much reduced, even without any cut on $M_{\nu_\ell\bar{\nu}_\ell}$. Nevertheless, the resonant calculation, either with or without OSP, gives a cross section which is 8% smaller than the full one, at variance with the case of final state W's [16].

So far we have considered a partonic process which receives contribution from 4Z amplitudes. We now perform an analogous study for $u\,s \to c\,d\,e^-e^+\mu^-\mu^+$, which receives contribution from 2W2Z amplitudes. The chosen kinematic cuts are identical to those detailed above. Numerical results are shown in table 5 for different choices of the cut Δ_M on both lepton pair invariant masses around the Z pole mass, i.e. $|M_{e^+e^-} - M_Z| < \Delta_M$ and $|M_{\mu^+\mu^-} - M_Z| < \Delta_M$. If no restriction on $|M_{\ell^+\ell^-} - M_Z|$ is imposed, the resonant

$\boldsymbol{\Delta_M}$	**FULL**	**RES OSP**	**RES NO OSP**
$u\,u \to u\,u\,\nu_e\,\bar\nu_e\,\nu_\mu\,\bar\nu_\mu$ (4Z)			
∞ (no cut)	0.5580(1)	0.5113(2)	0.5165(2)

Table 4. Cross sections (ab) for $u\,u \to u\,u\,\nu_e\bar\nu_e\nu_\mu\bar\nu_\mu$. All diagrams are taken into account for the full calculation (FULL), while only double resonant diagrams contribute to the two rightmost columns, with (RES OSP) and without (RES NO OSP) projection. Selection cuts are: $p_t^j > 20\,\text{GeV}$, $|\eta_j| < 5.5$, $M_{jj} > 600\,\text{GeV}$, $|\Delta\eta_{jj}| > 3.6$, $M_{4\ell} > 300\,\text{GeV}$.

$\boldsymbol{\Delta_M}$	**FULL**	**RES OSP**	**RES NO OSP**
$u\,s \to c\,d\,e^-\,e^+\,\mu^+\,\mu^-$ (2W2Z)			
∞ (no cut)	2.680(3)	2.483(3)	3.245(8)
30 GeV	2.457(3)	2.410(3)	2.432(2)
5 GeV	1.824(3)	1.822(4)	1.823(6)

Table 5. Cross sections (ab) for $u\,s \to c\,d\,e^-e^+\mu^-\mu^+$, for $|M_{\ell^+\ell^-} - M_Z| < \Delta_M$ $(\ell = e, \mu)$. All diagrams are taken into account for the full calculation (FULL), while only double resonant diagrams contribute to the two rightmost columns, with (RES OSP) and without (RES NO OSP) projection. Selection cuts are: $p_t^j > 20\,\text{GeV}$, $|\eta_j| < 5.5$, $M_{jj} > 600\,\text{GeV}$, $|\Delta\eta_{jj}| > 3.6$, $M_{4\ell} > 300\,\text{GeV}$, $M_{\ell^+\ell^-} > 40$ GeV.

$\boldsymbol{\Delta_M}$	**FULL**	**RES OSP**	**RES NO OSP**
$u\,s \to d\,c\,\nu_e\,\bar\nu_e\,\nu_\mu\,\bar\nu_\mu$ (2W2Z)			
∞ (no cut)	9.888(8)	9.758(9)	12.66(4)

Table 6. Cross sections (ab) for $u\,s \to d\,c\,\nu_e\,\bar\nu_e\,\nu_\mu\,\bar\nu_\mu$, for $|M_{\nu_\ell\bar\nu_\ell} - M_Z| < \Delta_M$ $(\ell = e, \mu)$. All diagrams are taken into account for the full calculation (FULL), while only double resonant diagrams contribute to the two rightmost columns, with (RES OSP) and without (RES NO OSP) projection. Selection cuts are: $p_t^j > 20\,\text{GeV}$, $|\eta_j| < 5.5$, $M_{jj} > 600\,\text{GeV}$, $|\Delta\eta_{jj}| > 3.6$, $M_{4\ell} > 300\,\text{GeV}$, $M_{\ell^+\ell^-} > 40$ GeV.

calculation (RES NO OSP) overestimates the full cross section by more than 20%. If OSP are applied, the cross section becomes 7% smaller than the full one: OSP play a different role in 2W2Z amplitudes, as they seem to regularize partially the gauge violating double resonant calculation, and the remaining discrepancy with respect to the full result is due to the γ coupling to charged leptons which is the main missing contribution in this setup. This is confirmed by the cross sections obtained for neutrinos in the final state, shown in table 6. In this case, since photons do not couple to neutrinos, the OSP result provides a good description of the full one (-1%). The resonant computation without OSP doesn't provide a trustworthy prediction (+30%). Turning back to the four charged leptons case, if a cut on $|M_{\ell^+\ell^-} - M_Z|$ is applied for both lepton pairs (see last two lines of table 5), ZZ resonant diagrams reproduce accurately the full result, both with and without OSP. For a very sharp cut (5 GeV), the full result is reproduced at the per mill level.

Other relevant processes contributing to ZZ scattering at the LHC are the mixed ones, which receive contributions both from 4Z and from 2W2Z amplitudes. We have checked

Δ_M	FULL	RES OSP	RES NO OSP
$u\, d \to u\, d\, e^-\, e^+\, \mu^+\, \mu^-$ (mixed)			
∞ (no cut)	20.09(2)	18.62(2)	24.67(4)
30 GeV	18.45(3)	18.08(3)	1.826(2)
5 GeV	13.69(2)	13.65(4)	1.362(2)

Table 7. Cross sections (ab) for $u\, d \to u\, d\, e^- e^+ \nu_\mu \mu^+$, for $|M_{\ell^+\ell^-} - M_Z| < \Delta_M$ ($\ell = e, \mu$). All diagrams are taken into account for the full calculation (FULL), while only double resonant diagrams contribute to the two rightmost columns, with (RES OSP) and without (RES NO OSP) projection. Selection cuts are: $p_t^j > 20$ GeV, $|\eta_j| < 5.5$, $M_{jj} > 600$ GeV, $|\Delta\eta_{jj}| > 3.6$, $M_{4\ell} > 300$ GeV, $M_{\ell^+\ell^-} > 40$ GeV.

Δ_M	FULL	RES OSP	RES NO OSP
$u\, s \to d\, s\, e^-\, e^+\, \nu_\mu\, \mu^+$ (WZWZ)			
∞ (no cut)	2.897(3)	2.746(4)	3.776(3)
30 GeV	2.701(2)	2.667(2)	2.686(2)
5 GeV	2.064(2)	2.060(3)	2.059(3)

Table 8. Cross sections (ab) for $u\, s \to d\, s\, e^-\, e^+\, \nu_\mu\, \mu^+$, for $|M_{e^+e^-} - M_Z| < \Delta_M$ and $|M_{\mu^+\nu_\mu} - M_W| < \Delta_M$. All diagrams are taken into account for the full calculation (FULL), while only double resonant diagrams contribute to the two rightmost columns, with (RES OSP) and without (RES NO OSP) projection. Selection cuts are: $p_t^j > 20$ GeV, $|\eta_j| < 5.5$, $M_{jj} > 600$ GeV, $|\Delta\eta_{jj}| > 3.6$, $M_{4\ell} > 300$ GeV, $M_{\ell^+\ell^-} > 40$ GeV.

that for such partonic channels the 2W2Z contribution is dominant, the 4Z one accounts for a few percent of the total, and the interference between the two sets of contributions is negligible. The numerical results in table 7 show that, in the presence of a reasonable cut on $M_{\ell^+\ell^-}$ around M_Z, the double resonant calculation describes accurately the full one.

We remark that, simulating ZZ scattering at the LHC including all possible partonic processes, the mixed ones account for 80% of the total cross section, pure 2W2Z processes account for more than 18%, and 4Z processes give a very small contribution (order 1%). This gives us confidence that double resonant diagrams provide reliable predictions, provided that a reasonable cut is imposed on $|M_{\ell^+\ell^-} - M_Z|$, both with and without OSP.

3.2 WZ processes

We now investigate how well resonant diagrams can reproduce full results in the WZ scattering channel. For this purpose we consider a single partonic process which features three charged leptons and a neutrino in the final state, namely $u\, c \to u\, s\, e^+ e^- \mu^+ \nu_\mu$. We apply exactly the same cuts as those applied for ZZ.

We show in table 8 the total cross sections corresponding to a few representative cuts, Δ_M, on the difference between the invariant mass of the decay particles and the vector boson mass. We require $|M_{\mu^+\nu_\mu} - M_W| < \Delta_M$ and $|M_{e^+e^-} - M_Z| < \Delta_M$, both with full matrix elements, and selecting only WZ resonant diagrams (with or without OSP).

In the absence of invariant mass restrictions on lepton pairs, the OSP cross section is 5% smaller than the full one, as a result of the unconstrained $M_{e^+e^-}$ which can be far from the Z pole mass (but $M_{\ell^+\ell^-} > 40$ GeV), where photons play an important role. The resonant calculation without OSP is far from providing reliable results in this situation (+30% w.r.t. the full cross section). In the presence of the cuts $|M_{e^+e^-} - M_Z| < 30$ GeV and $|M_{\mu^+\nu_\mu} - M_W| < 30$ GeV, resonant calculations underestimate the full result by only 1%. Making the invariant mass cuts even sharper (5 GeV), the resonant calculation describes perfectly (0.1% accuracy) the full result, both with and without On Shell projections. The conclusions we can draw for WZ are very similar to those for 2W2Z processes in ZZ scattering, apart from smaller effects related to γ decay, since WZ features only one opposite charge, same flavour lepton pair in the final state. However, differently from ZZ, in fully leptonic WZ scattering imposing a cut on $M_{\ell\nu_\ell}$ is physically unfeasible, thus we have to work out an alternative procedure to separate resonant contributions, which allows to avoid any cut on $M_{\ell\nu_\ell}$.

A possible way to avoid cuts on the $\ell^+\nu_\ell$ pair invariant mass consists in performing an On Shell projection on the W boson. This procedure is rather different from the double On Shell projections introduced above.

We select only W resonant diagrams (single-W-resonant and double resonant), dropping all the other contributions, which cannot be interpreted as the production of a W times its leptonic decay. The single On Shell projection (OSP1, for brevity) procedure consists in projecting on mass shell the numerator of the W resonant amplitude, leaving the Breit Wigner modulation untouched. In formulas,

$$
\begin{aligned}
\mathcal{A} &= \mathcal{A}_{\text{res}} + \mathcal{A}_{\text{nonres}} \\
&= \sum_\lambda \left[\frac{\mathcal{A}^{\mathcal{P}}_\mu(q_1, q_2; k, \{p_i\})\, \varepsilon^\mu_\lambda(k)\, \varepsilon^{*\nu}_\lambda(k)\, \mathcal{A}^{\mathcal{D}}_\nu(k, \{l_1, l_2\})}{k^2 - M_W^2 + i\Gamma_W M_W} \right] + \mathcal{A}_{\text{nonres}} \\
&\to \sum_\lambda \left[\frac{\mathcal{A}^{\mathcal{P}}_\mu(\bar{q}_1, \bar{q}_2; \bar{k}, \{p_i\})\, \varepsilon^\mu_\lambda(\bar{k})\, \varepsilon^{*\nu}_\lambda(\bar{k})\, \mathcal{A}^{\mathcal{D}}_\nu(\bar{k}, \{\bar{l}_1, \bar{l}_2\})}{k^2 - M_W^2 + i\Gamma_W M_W} \right] = \mathcal{A}_{\text{OSP1}}, \qquad (3.1)
\end{aligned}
$$

where q_1, q_2 are the initial parton momenta, k is the W momentum, l_1, l_2 are the W decay product momenta and $\{p_i\}$ are the momenta of the other final state particles. Barred momenta are the projected ones, in particular, $\bar{k}^2 = M_W^2$.

The projection procedure is not uniquely defined, since different sets of physical quantities can be kept unmodified. Our choice is to preserve:

1. the space like components of the W boson momentum in the laboratory reference frame,

2. the direction of the leptonic decay products momenta in the W rest frame,

3. the four momenta of all other final state particles (system X).

Since k, the off shell momentum of the W, is projected to the on shell momentum $\bar{k}$, while the other final state particles (X) are left untouched, the recoil $\Delta k = k - \bar{k}$ must be absorbed by the initial state partons ($q_1, q_2 \to \bar{q}_1, \bar{q}_2$).

$\mathbf{\Delta_M}$	**FULL**	**OSP1-W**	**OSP1-Z**
$u\ s \to d\ s\ e^-\ e^+\ \nu_\mu\ \mu^+$ (WZWZ)			
∞ (no cut)	2.897(3)	2.880(4)	2.752(3)
$30\,\mathrm{GeV}$	2.749(3)	2.741(4)	2.707(3)
$5\,\mathrm{GeV}$	2.359(3)	2.357(2)	2.354(3)

Table 9. Cross sections (ab) for $u\ s \to d\ s\ e^-\ e^+\ \nu_\mu\ \mu^+$, for $|M_{e^+e^-} - M_Z| < \Delta_M$. All diagrams are taken into account for the full calculation (FULL), only $W(Z)$ resonant diagrams contribute to the approximate calculation with OSP1-W(Z). Selection cuts are: $p_t^j > 20\,\mathrm{GeV}$, $|\eta_j| < 5.5$, $M_{jj} > 600\,\mathrm{GeV}$, $|\Delta\eta_{jj}| > 3.6$, $M_{4\ell} > 300\,\mathrm{GeV}$, $M_{\ell^+\ell^-} > 40$ GeV.

The same procedure can be applied when separating Z resonant diagrams. In this case, it amounts to selecting single-Z-resonant and double resonant diagrams, and then projecting on shell the Z boson.

To evaluate how well OSP1 results reproduce the full matrix element ones, we have computed the same cross sections of table 8 without any cut on $M_{\mu^+\nu_\mu}$. We have performed the calculation in three different ways: including all contributions (FULL), applying OSP1 on W resonant diagrams (OSP1-W), and applying OSP1 on Z resonant diagrams (OSP1-Z). Numerical results are shown in table 9.

Both in the absence and in the presence of cuts on $|M_{e^+e^-} - M_Z|$, the OSP1-W calculation provides predictions which are impressively close to the full ones (less than 0.7% differences). The issues related to the Z resonant part of the amplitude are absent, since all the contributions relevant for the description of the e^+e^- pair are included both in the full and in the OSP1-W calculation.

When applying OSP1 to Z resonant diagrams, the situation is slightly different. When leaving $|M_{e^+e^-} - M_Z|$ unconstrained, the approximate result is 5% smaller than the full, and very similar to the result obtained applying double On Shell projections (RES OSP) on double resonant diagrams (see second column, first line of table 8). The 5% discrepancy can be traced back (exactly as for double OSP) to the missing photon decay diagrams, which give non negligible contributions to the cross section. When applying a reasonable cut on $|M_{e^+e^-} - M_Z|$, the OSP1-Z result agrees with the full one within 1%. The sharper the cut, the better the agreement.

We stress that the OSP1-W(Z) results presented in table 9 assume that we select only single $W(Z)$ resonant and double resonant diagrams. This would be enough to separate polarizations of a single vector boson at a time. Nevertheless, with a view to separating polarizations for both vector bosons, it is even possible to treat only WZ double resonant contributions with OSP1 to describe the full result with reasonable accuracy, still avoiding cuts on $M_{\ell\nu_\ell}$. This can be done performing OSP1-W, and imposing a cut on $|M_{\ell^+\ell^-} - M_Z|$. The results obtained with this approximation in the presence of a 30 and 5 GeV cut on $|M_{\ell^+\ell^-} - M_Z|$ are almost identical to those shown in the rightmost column of table 9.

In conclusion, the OSP1 procedure provides an alternative approach to separate and treat $W(Z)$ resonant diagrams in WZ scattering, which reproduces correctly the full results in the presence of a reasonable cut on $|M_{\ell^+\ell^-} - M_Z|$, and avoiding cuts on $|M_{\ell\nu_\ell} - M_W|$.

4   *ZZ* scattering

The cross section for *ZZ* production in VBS has been measured by the CMS Collaboration in the fully leptonic channel [1]. In the fiducial region, at 13 TeV, it is less than 1 *fb*. Therefore, a detailed investigation of this process, even with the full luminosity of LHC Run 2, will be impossible. The high luminosity run of the LHC, with an integrated luminosity of about 3 ab^{-1}, is more promising and will hopefully allow for a separation of the longitudinal cross section in this channel [6, 7]. The four charged leptons in the final state enable a precise reconstruction of the *Z* decays and of their angular distributions. Furthermore, reducible backgrounds are small.

The $\gamma\gamma$ and γZ contributions, already mentioned in previous sections, can be controlled requiring the $\ell^+\ell^-$ invariant mass to be close to the *Z* pole mass: an experimentally viable cut is $|M_{\ell^+\ell^-} - M_Z| < 15$ GeV.

4.1   Setup of the simulations

We consider the process $pp \to jje^+e^-\mu^+\mu^-$ at the LHC@13 TeV. All simulations have been performed at parton level with PHANTOM [23, 24], employing NNPDF30_lo_as_0130 PDFs, with factorization scale $\mu = M_{4\ell}/\sqrt{2}$, in coherence with ref. [16], and as suggested in section I.8.3 of ref. [25].

We consider tree level electroweak contributions only ($\mathcal{O}(\alpha^6)$) and neglect partonic processes involving *b* quarks, which account for less than 0.5% of the total cross section.

The following set of kinematic cuts is applied for all results presented in this section:

- maximum jet rapidity, $|\eta_j| < 5$;

- minimum jet transverse momentum, $p_t^j > 20$ GeV;

- minimum invariant mass of the system of the two tagging jets, $M_{jj} > 500$ GeV;

- minimum rapidity separation between the two tagging jets, $|\Delta\eta_{jj}| > 2.5$;

- maximum difference between the invariant mass of each charged lepton pair (same flavor, opposite sign) and the *Z* pole mass, $|M_{\ell^+\ell^-} - M_Z| < 15$ GeV;

- minimum invariant mass of the four charged lepton system, $M_{4\ell} > 200$ GeV.

In section 4.3, in addition to those detailed above, transverse momentum and rapidity cuts are imposed on charged leptons kinematics: $p_t^\ell > 20$ GeV, $|\eta_\ell| < 2.5$.

Requiring the invariant mass of the four lepton system to be larger than 200 GeV, shields our results from the Higgs peak and selects the large diboson invariant mass region which is the most interesting one for studying the EWSB mechanism. We have preferred a mild cut which gives us more flexibility in the search for observable signatures and makes it easier to compare with the *WW* channel results in ref. [16], where the On Shell projection procedure forces the invariant mass of the four leptons to be larger than $2 M_W$.

Cross sections [ab]	
$ZZ \rightarrow ZZ$	0.979(2) (0.8%)
$WW \rightarrow ZZ$	24.73(3) (20.2%)
mixed	96.70(5) (79%)
total	122.41(9) (100%)

Table 10. Cross sections (ab) for the VBS ZZ production in the absence of lepton cuts. The mixed contribution refers to partonic subprocesses which include both $ZZ \rightarrow ZZ$ and $WW \rightarrow ZZ$ scattering subdiagrams. In parentheses we show the relative fractions.

4.2 Single polarized results and their validation in the absence of lepton cuts

In this section we provide Standard Model predictions for polarized ZZ scattering, in the absence of p_t and η cuts on charged leptons, and validate the results against the polarization information which can be extracted from the full distributions. In the following we only separate the polarized components of the Z which decays to e^+e^-. The Z which decays to $\mu^+\mu^-$ is always unpolarized.

Following the conclusions of section 3, in order to define polarized signals, we select only double resonant ZZ diagrams and impose $|M_{\ell^+\ell^-} - M_Z| < 15\,\text{GeV}$ for each lepton pair, without performing any on shell projection of the intermediate Z bosons, since this would be numerically irrelevant.

The total cross section obtained from the full matrix element is 122.41(9) ab. In table 10 we show the total cross sections corresponding to the underlying scattering reactions.

We observe that the partonic processes embedding only $ZZ \rightarrow ZZ$ account for less than 1% of the total. Furthermore, we have shown in section 3 that for mixed $e^+e^-\mu^+\mu^-$ processes the contribution of 4Z amplitudes account for less than 1% and that the interference between 4Z and 2W2Z amplitudes is negligible. Therefore, when including all partonic processes, any effect of γ/Z mixing is very small.

First, we investigate how well the different approximations compare with the full result in the unpolarized case. The unpolarized cross section obtained selecting only resonant diagrams is 121.48(8) ab, which reproduces the full cross section within 1%. If, in addition, we perform On Shell projections on resonant contributions, the approximate cross section is 121.44(8) ab. Since On Shell projections do not improve the approximate calculation, we do not apply them for ZZ in the following.

We now consider polarized signals. As lepton cuts are not applied, the incoherent sum of polarized cross sections (121.52(5) ab) reproduces perfectly their coherent sum presented above (121.48(8) ab). The results for a polarized Z are shown in table 11.

In order to validate the separation of polarized components, we compare the polarized cross sections obtained with the Monte Carlo with the results which, in the absence of lepton cuts, can be extracted from the full unpolarized $\cos\theta_{e^-}$ distributions. θ_{e^-} is the angle, in the correspondent Z rest frame, between the electron direction and the Z direction in the lab frame. As a consequence of eq. (2.4), each polarized decay cross section of a Z can be simply determined as it is a superposition of the first three Legendre polynomials.

Polarized cross sections [ab]	
longitudinal	32.60(2)
left handed	56.55(4)
right handed	32.37(2)
sum	121.52(5)

Table 11. Polarized cross sections (ab) for the VBS ZZ production in the absence of lepton cuts.
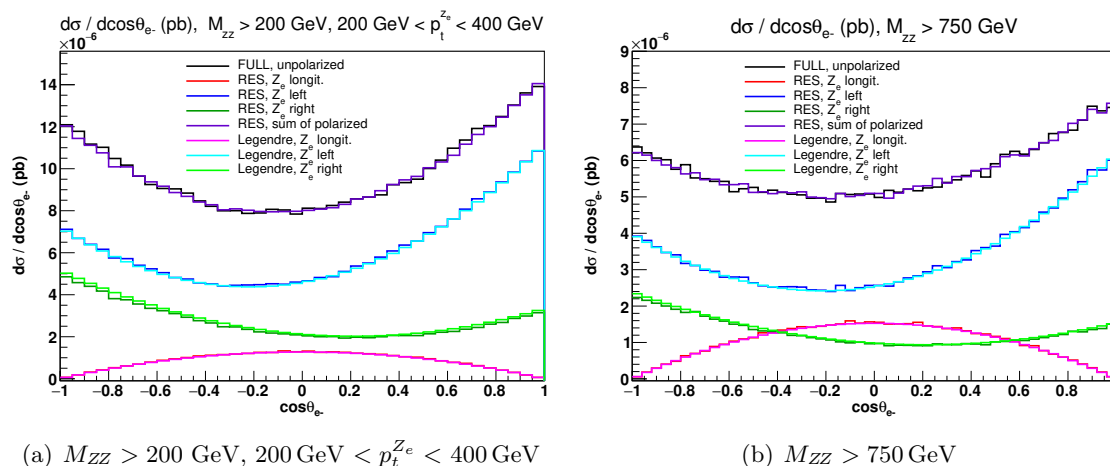

(a) $M_{ZZ} > 200\,\mathrm{GeV}$, $200\,\mathrm{GeV} < p_t^{Ze} < 400\,\mathrm{GeV}$

(b) $M_{ZZ} > 750\,\mathrm{GeV}$

Figure 3. ZZ scattering: $\cos\theta_{e^-}$ distributions in two different kinematic regions, in the absence of leptonic cuts, for a polarized Z decaying into e^+e^-. The pink, azure and light green curves represent respectively the longitudinal, left and right contributions obtained by expanding the full angular distribution (black curve) on the first three Legendre polynomials. The red, blue and dark green histograms represent respectively the longitudinal, left and right contributions computed with polarized amplitudes. The Z decaying to $\mu^+\mu^-$ is unpolarized.

In figure 3 we show the $\cos\theta_{e^-}$ distributions in two kinematic regions which are most sensitive to new physics, namely at large boson p_t and large mass of the diboson system.

In both figures, the full distribution is shown in black. The longitudinal, left and right distributions obtained with the Monte Carlo polarized amplitudes are shown in red, blue and dark green, respectively. The violet curve is their sum. The pink, cyan and light green curves represent the polarized distributions obtained projecting the full distribution onto the first three Legendre polynomials. The agreement between Monte Carlo polarized signals and the corresponding Legendre projections results is good, both for the total cross sections and for the distribution shapes. The discrepancy between the full distributions and the sum of polarized results, though $\lesssim 3\%$ bin per bin in all the analyzed kinematic region, are slightly larger than those observed in WW scattering. This may be due to γ contributions, as well as to non resonant contributions, which are missing in the resonant approximate calculation. However, the agreement is satisfactory, therefore we can proceed to study polarized signals in the presence of lepton cuts.

Polarized cross sections [ab]	
longitudinal	16.19(1)
left handed	26.76(2)
right handed	15.95(1)
sum	58.91(2)

Table 12. Polarized cross sections (ab) for the VBS ZZ production in the presence of lepton cuts.

4.3 Effects of lepton cuts on polarized distributions

The inclusion of p_t and η cuts on charged leptons defines a fiducial region where it is possible to reconstruct the entire final state. The total cross section computed with full matrix elements is $61.02(4)\,ab$. The result of the computation including only double resonant diagrams is $60.59(4)\,ab$ which reproduces the full result with 1% accuracy, meaning that, also in this case, non resonant and γ contributions are very small. Applying On Shell projections we get $60.46(4)\,ab$, showing that they can be avoided, even in the presence of the full set of lepton cuts, which spoils the cancellation of interference terms among different polarization states. This introduces an additional source of discrepancy between the incoherent sum of polarized distributions and the full unpolarized distribution. This is quantified in table 12.

The incoherent sum of polarized total cross sections underestimates the full cross section by 3.5%: interferences among polarization modes are small but non negligible.

These interferences are even more evident in differential cross sections. In figure 4(a) we show the distributions in $\cos\theta_{e^-}$, which are to be compared with those in figure 3. The effect of p_t and η cuts on charged leptons is to deplete the forward and backward regions at $\theta = 0, \pi$: this mainly induces a strong modification of the transverse distribution shapes, which would feature a maximum in those regions, if lepton cuts were not applied. The sum of the three polarized distributions (violet curve) reproduces the full result fairly well. There is an essentially constant 4% shift in each bin which reflects the overall cross section difference.

In figure 4(b) we present the differential cross sections of the four lepton system invariant mass: the left component is the largest, with the exception of the very first bin, and this effect increases at large invariant masses, where the longitudinal and right contributions each accounts for about 10% of the full cross section. A similar behaviour can be observed in the distribution of the transverse momentum of the Z boson which decays into e^+e^- (figure 4(c)): the longitudinal component features a peak around 40 GeV, then it decreases much faster than the transverse ones.

The Z pseudorapidity is shown in figure 4(d). The longitudinal component has the usual dip in the central region, while its tails at $|\eta_{Z_e}| > 2$ are larger than the transverse ones.

In general, the left and right distributions are characterized by a very similar shape for many kinematic distributions (figures 4(b), 4(c) and 4(d)), with the obvious exception of the $\cos\theta_{e^-}$ distribution.

The incoherent sum of polarizations at the amplitude level works reasonably well even in the presence of a complete set of kinematic cuts, provided a sufficiently narrow window
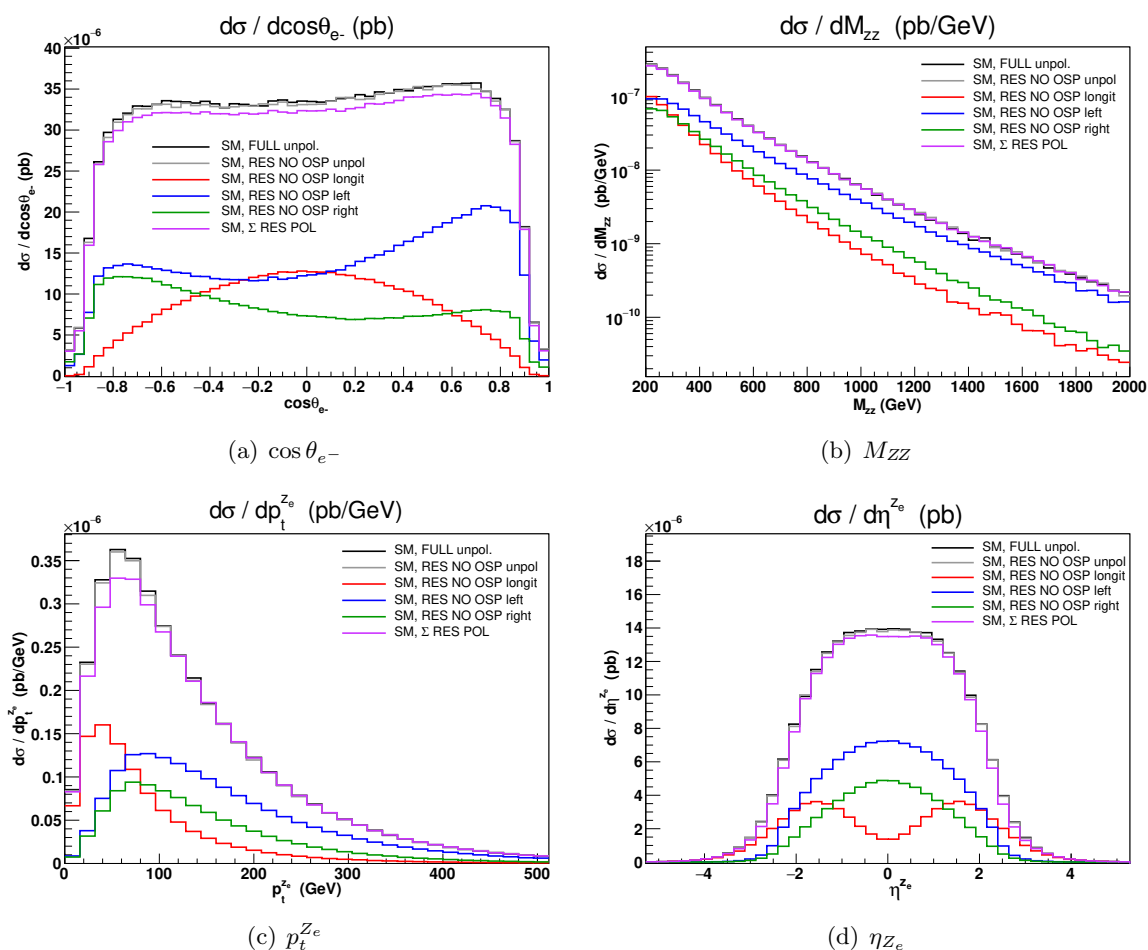
Figure 4. ZZ scattering: polarized distributions in the presence of lepton cuts, obtained integrating the polarized amplitudes squared. The Z decaying to e^+e^- is polarized, the one decaying to $\mu^+\mu^-$ is unpolarized. The sum of polarized components (violet curve) is compared against the full unpolarized distribution (black curve).

for the $\ell^+\ell^-$ pair invariant mass around M_Z is selected. The longitudinal component accounts for 26.5% of the total. The left and right handed contributions account for 43.9% and 26.1%, respectively. Interferences are not negligible, about 3.5%, and should be taken into account in experimental analyses.

For analogous predictions in the presence of BSM dynamics, and a discussion on the model independent extraction of Z polarization fractions from LHC data, we refer to section 7.

5 WZ scattering

The measurements by the ATLAS and CMS Collaborations [4, 5], as well as the recent calculation of the NLO EW and QCD corrections [26] and of parton shower effects [27] highlight a growing interest in the WZ scattering channel. In this section we investigate

the phenomenology of polarized W^+Z scattering in the fully leptonic decay channel at the LHC. We consider both the case in which the W^+ boson has definite polarization and the Z is unpolarized, and the case in which the Z boson has definite polarization and the W^+ is unpolarized.

The WZ channel is strongly sensitive to the EWSB mechanism, as it can be proved computing the Feynman diagrams of the tree level amplitude for on shell scattering between longitudinal bosons. Similarly to $WW \to ZZ$ and $WW \to WW$, pure gauge diagrams grow like s^2, while their sum grows linearly with s (more precisely with $t = s(1 - \cos\theta)$), violating perturbative unitarity at high energies. The Higgs contribution regularizes the full amplitude, restoring unitarity. The presence of a new resonance coupling to W and Z bosons or a modified Higgs sector would interfere with this delicate cancellation of large contributions, enhancing the longitudinal cross section at high energies.

The fully leptonic WZ scattering is more appealing than the WW channel because the presence of only one neutrino in the final state allows to reconstruct, at least approximately, the center of mass frame of the W boson. In the WW case the presence of two neutrinos makes the reconstruction impossible. The cross section for WZ production in VBS is expected to be larger than the ZZ one, enabling more accurate analyses with the LHC Run II luminosity.

5.1 Setup of the simulations

In the following, we consider the process $pp \to jje^+e^-\mu^+\nu_\mu$ at the LHC@13 TeV. We use the same PDF set and factorization scale described in 4.1. We only consider tree level electroweak contributions and neglect partonic processes involving b quarks, which account for less than 1.5% of the total cross section.

We have applied the following kinematic cuts:

- maximum jet rapidity, $|\eta_j| < 5$;

- minimum jet transverse momentum, $p_t^j > 20\,\text{GeV}$;

- minimum invariant mass of the two tagging jet system, $M_{jj} > 500\,\text{GeV}$;

- minimum rapidity separation between the two tagging jets, $|\Delta\eta_{jj}| > 2.5$;

- maximum difference between the invariant mass of the e^+e^- pair and the Z pole mass, $|M_{e^+e^-} - M_Z| < 15\,\text{GeV}$;

- minimum invariant mass of the four lepton system, $M_{WZ} > 200\,\text{GeV}$.

The results presented in section 5.3 include three additional cuts

- maximum charged lepton rapidity, $|\eta_\ell| < 2.5$;

- minimum charged lepton transverse momentum, $p_t^\ell > 20\,\text{GeV}$;

- minimum missing transverse momentum, $p_t^{\text{miss}} > 40$ GeV.
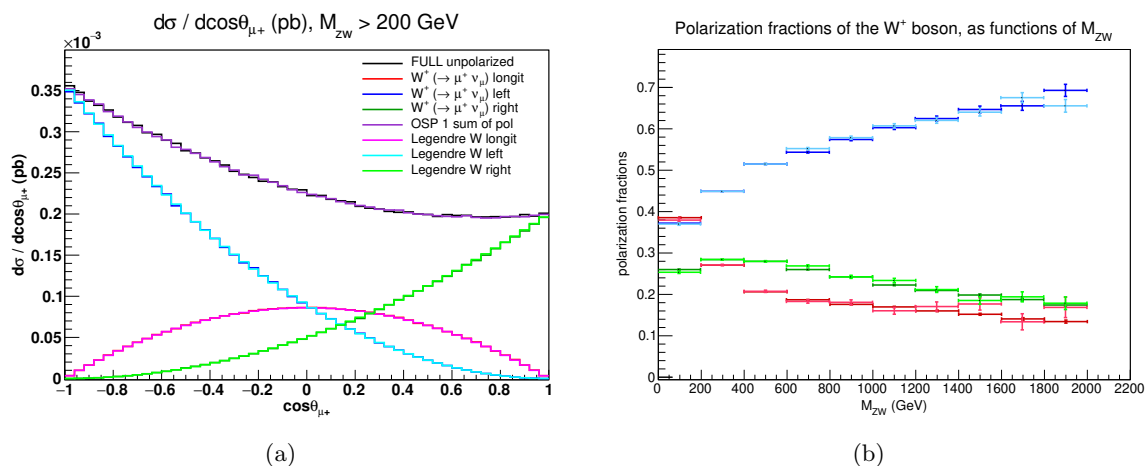
Figure 5. W^+Z scattering: $\cos\theta_{\mu^+}$ distributions for a polarized W^+, in the region $M_{WZ} > 200$ GeV (left), and polarization fractions as functions of M_{WZ} (right). Comparison between Monte Carlo distributions and results extracted from the full $\cos\theta_{\mu^+}$ distribution by projecting into the first three Legendre polynomials. No lepton cuts, no neutrino reconstruction.

In section 5.2 the M_{WZ} cut is imposed directly on the generated, not reconstructed, momenta. In section 5.3 the cut is applied after neutrino reconstruction. For more details on neutrino reconstruction the reader is referred to appendix A.

5.2 Single polarized results and their validation in the absence of lepton cuts

In order to verify that polarizations can be separated at the amplitude level while reproducing properly the full result, we consider the ideal kinematic setup in which no cut on charged leptons and neutrinos is applied, apart from $|M_{e^+e^-} - M_Z| < 15$ GeV and $M_{WZ} > 200$ GeV.

Following the discussion in section 3, in order to isolate the polarizations of the $W(Z)$ boson in W^+Z scattering, we select only the $W(Z)$ resonant diagrams (single and double resonant) out of the full set of contributions. Then we apply the OSP1-W(Z) projection on the $W(Z)$ boson, to avoid any cut on the $\mu^+\nu_\mu$ system invariant mass. We have shown that for Z resonant diagrams, OSP1 has no visible effect, but, nonetheless, we apply it for consistency. In all the following we will refer to OSP1-W(Z) projected $W(Z)$ resonant calculation simply as resonant calculation.

The full matrix element includes both resonant and non resonant diagrams, therefore in principle it would not be possible to cast the full $\cos\theta_\ell$ distribution in the form of eq. (2.4). On the contrary, the unpolarized resonant amplitude features a vector boson (either the W or the Z) which is radiated and then decays leptonically, making it possible to apply eq. (2.4). We have checked that the unpolarized resonant distributions describe accurately the full distributions. This enables to treat equivalently the full or the resonant $\cos\theta_\ell$ distributions by means of eq. (2.4).

The total cross section computed with full matrix elements is $486.4(2)\,ab$. The unpolarized OSP1-W resonant result is only 0.2% smaller. Similarly, the OSP1-Z resonant
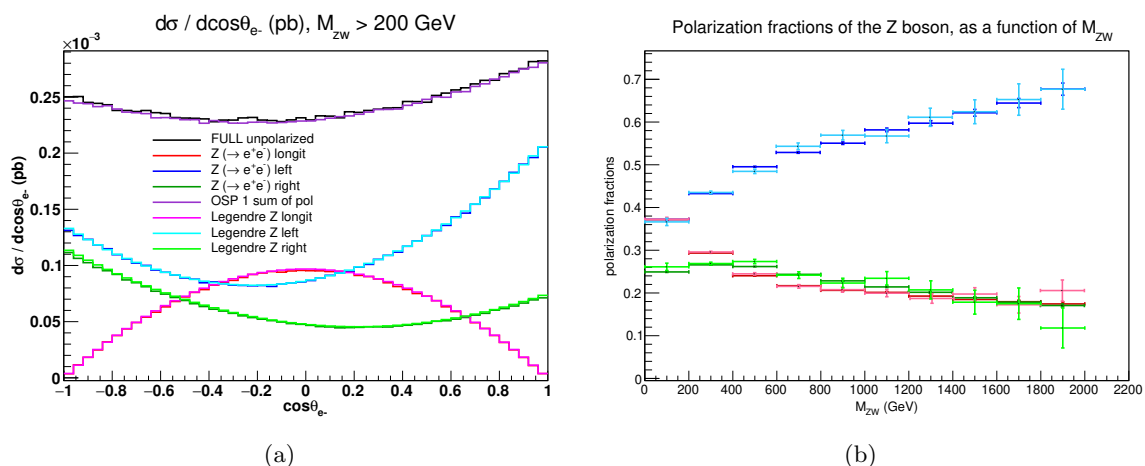
Figure 6. W^+Z scattering: $\cos\theta_{e^-}$ distributions for a polarized Z, in the region $M_{WZ} > 200$ GeV (left), and polarization fractions as functions of M_{WZ} (right). Comparison between Monte Carlo distributions and results extracted from the full $\cos\theta_{e^-}$ distribution by projecting into the first three Legendre polynomials. No lepton cuts, no neutrino reconstruction.

computation underestimates by 0.7% the full result. Differential distributions are also in good agreement. Discrepancies are smaller than 2% bin by bin.

We first separate the polarizations of the W^+ boson. In figure 5(a) we consider the $\cos\theta_{\mu^+}$ distributions in the full $M_{WZ} > 200$ GeV range in the absence of lepton cuts and without neutrino reconstruction.

The distributions obtained with polarized amplitudes (red, blue and dark green, for longitudinal, left and right polarization, respectively) are compared with the components extracted from the full distribution (magenta, azure and light green) by projecting onto the first three Legendre polynomials. The agreement is very good: both the normalization and the quadratic dependence on $\cos\theta_{\mu^+}$ is perfectly reproduced for each polarization state. We have performed the same study in several WZ invariant mass regions, and we have compared the polarization fractions extracted from the full result with the ratios of polarized Monte Carlo cross sections to the full cross section. The results are shown in figure 5(b). Error bars show the statistical uncertainties on the polarization fractions. The agreement is good in all invariant mass regions.

Very similar conclusions can be drawn when separating the polarization of the Z boson. We show in figure 6 the $\cos\theta_{e^-}$ distributions for a polarized Z boson in the $M_{WZ} > 200$ GeV region, as well as the polarization fractions as functions of the W^+Z invariant mass. Also for the Z decay, the polarized distributions extracted from the full result and those produced directly with the Monte Carlo are in very good agreement in all kinematic regions, both for the total rates, figure 6(b), and for the distribution shapes, figure 6(a).

5.3 Effects of lepton cuts and neutrino reconstruction on polarized distributions

In this section we present polarized differential distributions in the presence of lepton cuts and neutrino reconstruction for a number of relevant kinematic variables. The specific

Total cross sections [ab]		
	polarized W^+	polarized Z
longitudinal (res. OSP1)	33.21(3)	42.56(3)
left handed (res. OSP1)	96.31(8)	76.87(6)
right handed (res. OSP1)	30.93(2)	40.54(3)
sum of polarized	160.45(9)	159.97(8)
unpolarized (res. OSP1)	164.2(2)	164.0(2)
non res. effects	0.9(2)	1.1(2)
pol. interferences	3.8(2)	4.0(2)
full	165.1(1)	165.1(1)

Table 13. Polarized and unpolarized total cross sections (ab) for W^+Z scattering in the fiducial region (see section 5.1).

neutrino reconstruction scheme that is applied in the following (`CoM` + `transvMlv`) is described in appendix A. We provide results for a polarized W^+ produced in VBS together with an unpolarized Z boson, as well as for a polarized Z produced in association with an unpolarized W^+.

We start from the total cross section. In order to evaluate separately the effect of dropping the non resonant diagrams and the effect of neglected interferences among different polarization modes, we have computed the cross section with the full matrix element and with OSP1-W(Z) projected resonant diagrams (see section 3). The difference between these two results provides an estimate of non resonant effects. The difference between the resonant unpolarized cross section and the sum of the single polarized ones (either for a polarized W^+ or for a polarized Z) provides an estimate of the interference among polarizations, which is non zero because of the leptonic cuts. Numerical results are shown in table 13.

The resonant unpolarized calculation has been performed selecting single $W(Z)$ resonant diagrams, and then applying the corresponding single On Shell projection. In both cases non resonant effects are smaller than 1%, implying that the resonant approximation works rather well. Interference among polarization states amounts to 2.5%. We are going to show in section 7.1 that the largest interference is between the left polarization and the right one. The combination of the two effects give a 3% contribution to the full result, which is small but non negligible, and should be taken into account for a proper determination of polarized signals.

Concerning polarized total cross sections, the W^+ is mainly left handed (58.3%), while the longitudinal and right handed contributions are of the same order of magnitude (20.1% and 18.7%, respectively). For the Z boson, the left polarization is again the largest (46.6%) while the longitudinal and right components account respectively for 25.8% and 24.6%.

In figure 7 and figure 8 we present differential distributions for a variety of kinematic variables, which provide a more detailed description of the polarized signals. For each variable, we show single polarized distributions, their incoherent sum, and the distribution of the full result. In both figures we use the same color code: the full result is in black; the longitudinal, left and right single polarized distributions are in red blue and green
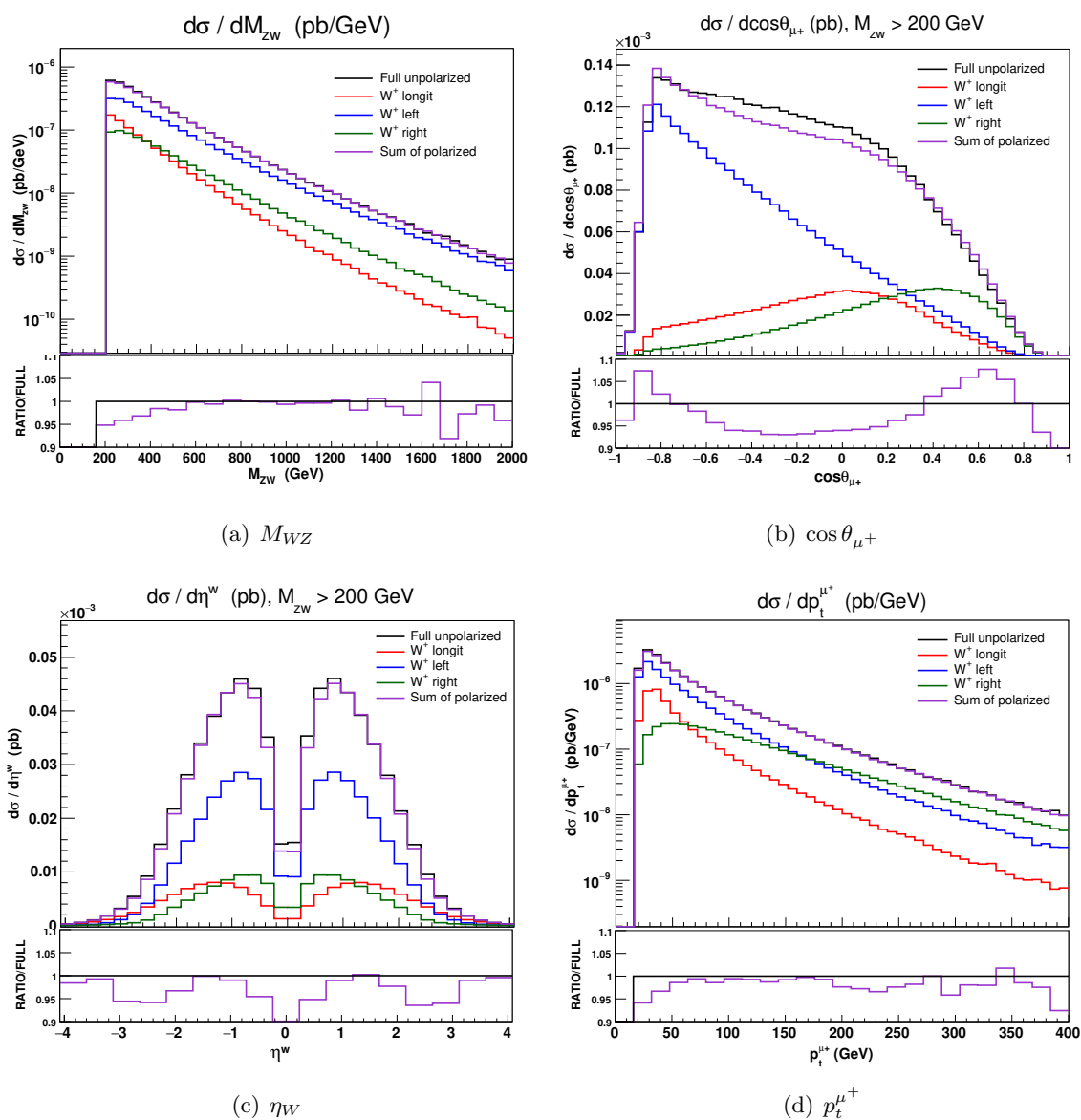
Figure 7. W^+Z scattering: differential cross sections for a polarized W^+ boson, in the presence of lepton cuts and neutrino reconstruction. We show the full result (black), the single polarized distributions (red: longitudinal, blue: left handed, green: right handed) and the incoherent sum of the polarized results (violet). The pull plot shows the ratio of the sum of polarized distributions to the full one.

respectively; the incoherent sum of the polarized results is in violet. Pull plots show the bin by bin ratio of the incoherent sum of polarized distributions to the full one.

In figure 7 we show distributions for a polarized W^+ boson. Figure 7(a) presents the distribution of the invariant mass of the four leptons. The interference and non resonant effects account for less than 5% of the full result (bin by bin) in the whole W^+Z invariant mass spectrum, up to fluctuations due to low statistics in the large mass region (figure 7(a)). The longitudinal fraction decreases rapidly with increasing energy. The left

handed component is the largest one over the whole range. For $M_{WZ} > 1600$ GeV it is about ten times larger than the longitudinal one.

The angular distributions in $\cos\theta_{\mu^+}$ are strongly affected by the neutrino reconstruction and the lepton cuts, as can be seen comparing figure 7(b) with figure 5(a). The difference is mainly due to the p_t cuts on the muon and the corresponding neutrino, which deplete the peaks at $\theta_{\mu^+} = 0, \pi$ of the transverse modes and make the longitudinal shape asymmetric. The sum of polarized distributions underestimates the full result by at most 5% bin by bin, apart from the regions $\cos\theta_{\mu^+} \approx -0.8$ and $\cos\theta_{\mu^+} \approx +0.7$, where the interferences become large and negative, inducing a discrepancy of about 8–10%.

In figure 7(c) we show distributions of the reconstructed W^+ pseudorapidity. Neutrino reconstruction leads to a marked depletion of the central region. Without neutrino reconstruction, the unpolarized and transverse distributions would have a maximum in $\eta_W = 0$. The longitudinal component is less affected since, even in the absence of neutrino reconstruction, it shows a dip in the central region. Interferences and non resonant effects account for less than 6% of the full result over all the pseudorapidity range, apart from the central bin where they reach 10%.

The transverse momentum of the muon (figure 7(d)) is minimally affected by neutrino reconstruction. The longitudinal component is of the same order of magnitude than the left handed one for p_t values slightly above the cut threshold, while for large values it decreases faster than the two transverse distributions. For $p_t^{\mu^+} > 160$ GeV the right handed component becomes larger than the left handed one. Interferences are small (less than 6% bin by bin) over the full range.

In figure 8, we present distributions for a polarized Z boson. The M_{WZ} distributions shown in figure 8(a) are very similar to those of figure 7(a), apart from a less pronounced difference between the longitudinal and the right handed contribution at large mass.

The variables related to the Z boson kinematics are not directly affected by neutrino reconstruction, apart from a small shift in the total cross section due to the minimum M_{WZ} cut.

In figure 8(b) we show how $\cos\theta_{e^-}$ distributions are affected by lepton cuts. This variable depends on the kinematics of two same flavour opposite sign charged leptons, whose p_t is cut at $20\,\mathrm{GeV}$: these symmetric cuts result in a less pronounced effect in the $\theta_{e^-} = 0, \pi$ regions depletion, if compared with the $\cos\theta_{\mu^+}$ distributions of figure 7(b), where the effects are more prominent due to an asymmetry in the p_t cuts on the two objects that reconstruct the W^+ ($p_t^{\mu^+} > 20$ GeV, $p_t^{\mathrm{miss}} = p_t^{\nu_\mu} > 40$ GeV). The incoherent sum of polarized $\cos\theta_{e^-}$ distributions reproduces quite well the full one: interferences and non resonant effects are roughly constant over the kinematic range, accounting for 4% of the full.

The η_Z distributions in figure 8(c) show larger interferences among polarization modes in the forward regions $2 < |\eta_Z| < 3$ where they account for 10% of the total. The longitudinal component features the typical depletion at $\eta_Z = 0$, where the transverse modes show a peak. The longitudinal fraction becomes larger than the transverse ones in the forward regions, for $\eta_Z > 2.5$.

In figure 8(d) we show the transverse momentum distributions of the electron. Interferences and non resonant effects are small ($\lesssim 5\%$ bin by bin). In contrast with the
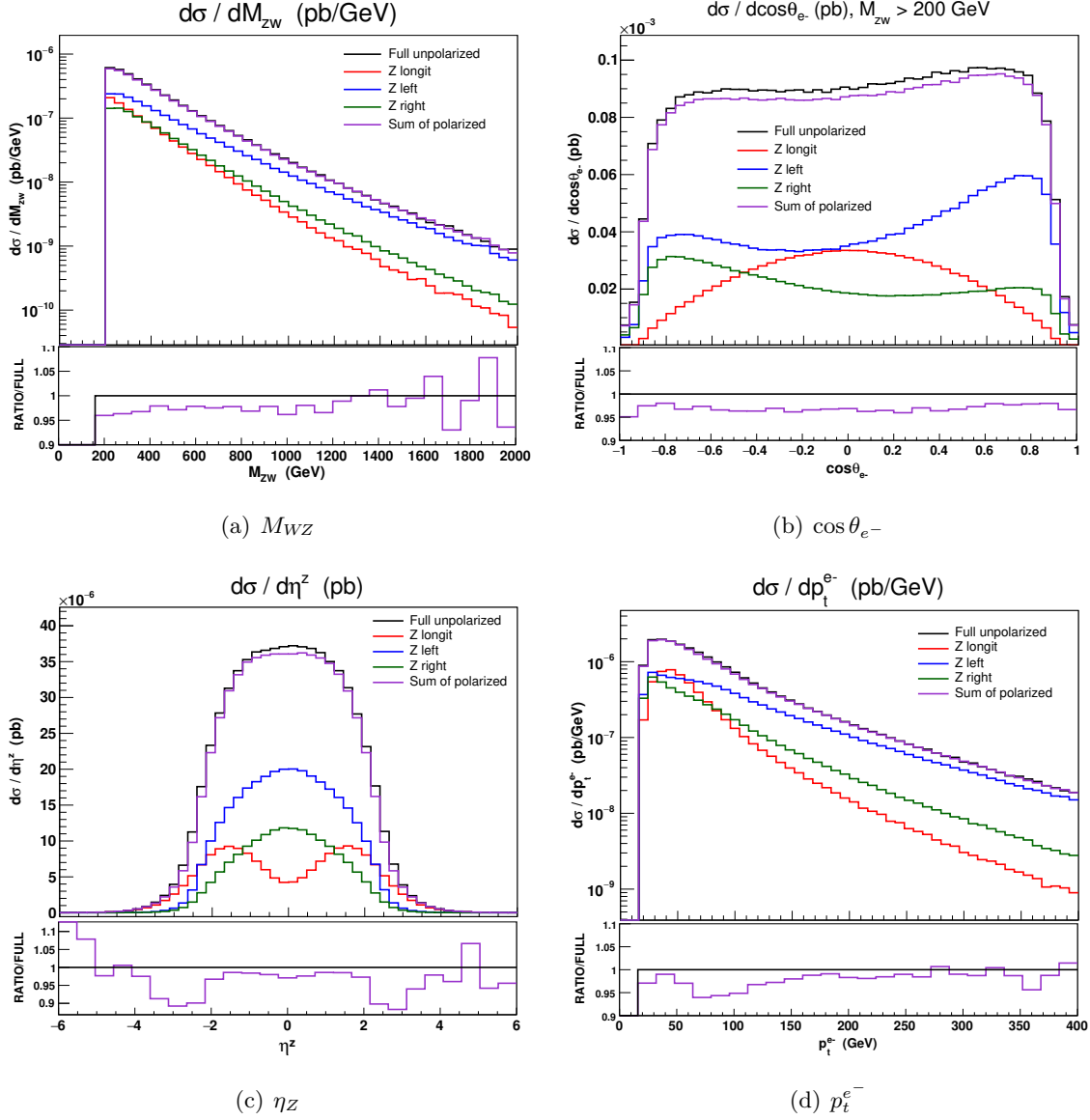
Figure 8. W^+Z scattering: differential cross sections for a polarized Z boson, in the presence of lepton cuts and neutrino reconstruction. We show the full result (black), the single polarized distributions (red: longitudinal, blue: left handed, green: right handed) and the incoherent sum of the polarized results (violet). The pull plot shows the ratio of the sum of polarized distributions to the full one.

W^+ case, the Z is mainly left handed at large p_t. In the soft p_t region the three polarizations are of the same order of magnitude. We have checked that if we allow for small WZ invariant masses ($M_{WZ} < 200$ GeV), the peak of the longitudinal component becomes more pronounced. In general, the longitudinal contribution decreases more rapidly than the transverse ones in the high energy, high p_t region.

In conclusion, the separation of polarized signals at the amplitude level gives reliable predictions both for a polarized W^+ and for a polarized Z, even in the presence of a realistic set of kinematic cuts and when neutrino reconstruction is applied. Interference and reconstruction effects are non negligible, but small (few percent) and well under control in our framework.

6   Polarized amplitudes and reweighting approach

Reweighting is an approximate procedure which has been widely used by experimental collaborations to obtain polarized samples, starting from unpolarized Monte Carlo events. It has been employed for the extraction of polarization fractions of W bosons [12, 13, 28], Z bosons [29] and top quarks [30]. In this section we evaluate how well the reweighting method can separate polarized samples and describe polarized distributions in the case of W^+Z scattering, by comparing its results with those presented in section 5, which have been obtained using polarized amplitudes computed by the Monte Carlo.

Let's consider a generic process which involves a W^+ boson decaying into leptons (similar considerations apply to the Z). The reweighting procedure is based on the partition of the W^+ boson phase space in two dimensional $\{p_t, \eta\}$ regions, as narrow as possible. In the absence of lepton cuts and neutrino reconstruction, polarization fractions $f_0^{(i)}$, $f_L^{(i)}$ and $f_R^{(i)}$ are computed in each $\{p_t^W, \eta_W\}$ region labelled by index i, expanding the full, unpolarized $\cos\theta_{\mu^+}$ distribution in Legendre polynomials (or, equivalently, fitting it with the distribution of eq. (2.4)). The unpolarized sample is then divided as follows. If an event belongs to region i and has $\cos\theta_{\mu^+} = x$, three weights are computed,

$$w_{0,L,R} = \frac{\frac{1}{\sigma}\frac{d\sigma}{dx}\Big|_{0,L,R}}{\frac{3}{4}(1-x^2)f_0^{(i)} + \frac{3}{8}(1-x)^2f_L^{(i)} + +\frac{3}{8}(1+x)^2f_R^{(i)}} \tag{6.1}$$

where,

$$\frac{1}{\sigma}\frac{d\sigma}{dx}\Big|_0 = \frac{3}{4}(1-x^2)f_0^{(i)}, \qquad \frac{1}{\sigma}\frac{d\sigma}{dx}\Big|_{L/R} = \frac{3}{8}(1\mp x)^2 f_{L/R}^{(i)}.$$

Finally, the event is assigned to the longitudinal, left or right polarized sample with probability w_0, w_L, w_R, respectively. The three samples are then analyzed separately, applying lepton cuts and performing neutrino reconstruction.

We have applied the reweighting method to $pp \to jje^+e^-\mu^+\nu_\mu$. In the absence of lepton cuts and neutrino reconstruction (see section 5.2), we have computed polarization

Polarized cross sections [ab], $M_{WZ} > 200\,\mathrm{GeV}$		
polarization	MC polarized	Reweighting
longit.	33.21(3)	41.02(3)
left	96.31(8)	95.97(2)
right	30.93(2)	27.87(3)

Table 14. Polarized total cross sections (ab) for W^+Z scattering in the region $M_{WZ} > 200$ GeV: results of the reweighting procedure compared with results of the MC calculation with polarized amplitudes. The full set of cuts and neutrino reconstruction are understood.
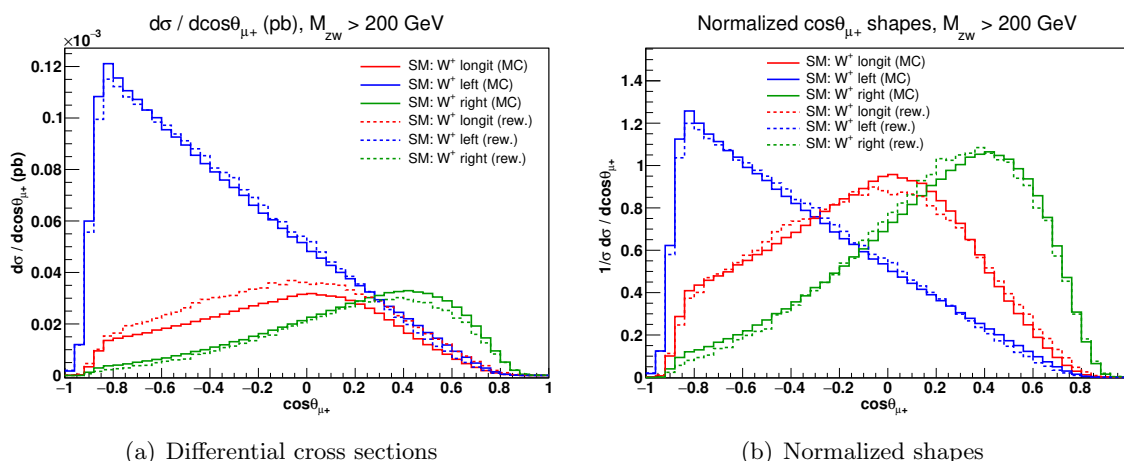

(a) Differential cross sections

(b) Normalized shapes

Figure 9. W^+Z scattering: polarized $\cos\theta_{\mu^+}$ distributions in the region $M_{WZ} > 200$ GeV. Results of the reweighting procedure compared with results of the MC calculation with polarized amplitudes. The full set of cuts and neutrino reconstruction are understood.

fractions for the full process with the following partitioning of the $\{p_t^W, \eta_W\}$ phase space, as done in ref. [28]:

- $p_t^W < 30\,\mathrm{GeV}$, $30\,\mathrm{GeV} < p_t^W < 60\,\mathrm{GeV}$, $60\,\mathrm{GeV} < p_t^W < 90\,\mathrm{GeV}$, $p_t^W > 90\,\mathrm{GeV}$;

- $|\eta_W| < 1$, $1 < |\eta_W| < 2$, $2 < |\eta_W| < 3$, $|\eta_W| > 3$.

In each region, we have separated the full unpolarized sample into three polarized samples, using the algorithm described above. Then we have applied the full set of leptonic cuts and performed neutrino reconstruction, obtaining approximate polarized distributions which can be compared with those presented in section 5.3. We have compared total cross sections (tables 14, 15) and reconstructed $\cos\theta_{\mu^+}$ differential distributions (figures 9, 10).

In the whole fiducial region ($M_{WZ} > 200$ GeV), the left polarized $\cos\theta_{\mu^+}$ distribution obtained with the reweighting procedure describes fairly well the analogous distribution obtained with polarized amplitudes, both in total cross section and in shape ($\sigma^{-1}\,d\sigma(X)/dX$). On the contrary, the longitudinal total cross section is overestimated by 23% and the right polarized cross section is underestimated by 10%, as shown in table 14. Even larger discrepancies show up when analyzing the $\cos\theta_{\mu^+}$ differential cross section and shape (figure 9).

Polarized cross sections [ab], $M_{WZ} > 500\,\text{GeV}$		
polarization	MC polarized	Reweighting
longit.	5.96(2)	9.94(4)
left	28.38(3)	25.49(3)
right	9.06(3)	8.13(3)

Table 15. Polarized total cross sections (ab) for W^+Z scattering in the region $M_{WZ} > 500$ GeV: results of the reweighting procedure compared with results of the MC calculation with polarized amplitudes. The full set of cuts and neutrino reconstruction are understood.

(a) Distributions

(b) Normalized shapes
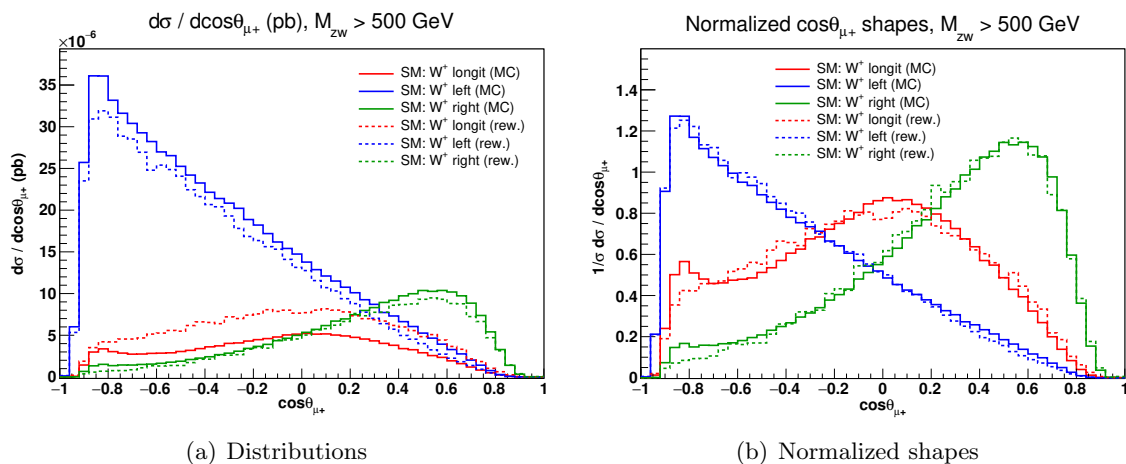
Figure 10. W^+Z scattering: polarized $\cos\theta_{\mu^+}$ distributions in the region $M_{WZ} > 500$ GeV. Results of the reweighting procedure compared with results of the MC calculation with polarized amplitudes. The full set of cuts and neutrino reconstruction are understood.

It is important to observe that the sum of the three cross sections obtained with polarized amplitudes (central column of table 14), is not equal to the full unpolarized cross section, since the interferences among polarizations account for 5% of the full result.

Interferences are completely neglected in the reweighting method (rightmost column of table 14). As a consequence, the sum of the three polarized cross sections is, by construction, equal to the full unpolarized one.

The inaccuracy of the reweighting procedure becomes even more evident at high energies, as figure 10 and table 15 show. For $M_{WZ} > 500$ GeV, the reweighting predictions are absolutely unreliable. In particular, the longitudinal cross section is overestimated by 70%, and the corresponding $\cos\theta_{\mu^+}$ shape is rather different from the Monte Carlo polarized prediction. At large diboson masses, the polarization interferences are smaller than at lower masses, however neglecting them contributes to the low precision of the reweighting method.

The main bottleneck of the reweighting procedure is represented by the phase space dependence of the polarization fractions. In the absence of lepton cuts, each polarization gives the same lepton angular distribution in the W rest frame in any phase space point. However, the relative weight of the three polarizations varies from point to point. When assigning a polarization state to a single event, the reweighting procedure assigns to each
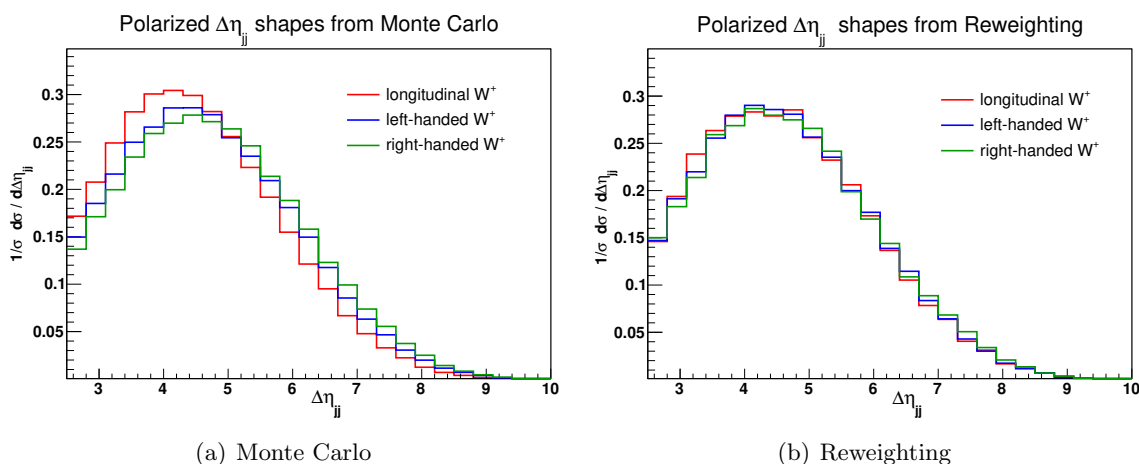
Figure 11. W^+Z scattering: $\Delta\eta_{jj}$ normalized distributions for a polarized W^+, obtained with polarized amplitudes (left side) and with the reweighting procedure (right side), in the region $60 \text{ GeV} < p_t^W < 90 \text{ GeV}, 1 < |\eta_W| < 2$, in the absence of lepton cuts and without neutrino reconstruction.

event belonging to a $\{p_t^W, \eta_W\}$ cell the average weight over the whole region. As a consequence, the reweighting method is not capable of reproducing the correct dependence on kinematic variables different from $\cos\theta_{\ell^+}$.

To show that this is the case even in the absence of lepton cuts and neutrino reconstruction, we have compared, in the region $60 \text{ GeV} < p_t^W < 90 \text{ GeV}, 1 < |\eta_W| < 2$, the longitudinal, left, and right distributions obtained from reweighting with those computed directly with polarized amplitudes, for a number of variables which do not depend on the decay products of the polarized W^+. In figure 11, we show the normalized distributions of the rapidity difference between the two tagging jets. The polarized shapes on the left, obtained with polarized amplitudes, are clearly different from each other: the longitudinal one is peaked at a smaller value of $\Delta\eta_{jj}$ than the two transverse components, and decreases faster in the distribution tail. The analogous polarized shapes from reweighting, on the right of figure 11, are similar to each other, confirming that, even when considering a small $\{p_t^W, \eta_W\}$ region, reweighting corresponds to averaging on the dependence on other variables, washing out the differences, even in the absence of leptonic cuts.

Also the η_W and p_t^W distributions cannot be described perfectly.

This becomes even more problematic when lepton cuts are imposed on the polarized samples, since selection cuts have different effects on different polarizations. The conceptual issue is that the polarized samples are obtained without lepton cuts, and then are analyzed in the presence of cuts. The computation of polarization fractions and the application of lepton cuts are non commuting procedures.

Notice that the correct description of all kinematic variables is mandatory for a Multi Variate Analysis.

We have shown that the reweighting method to separate an unpolarized event sample into three polarized samples provides only approximate predictions, which can be quite

far from being accurate, particularly at high energies. Therefore it would be better, both for phenomenological and for experimental analyses, to produce polarized event samples employing directly polarized amplitudes.

7 Extracting polarization fractions

In this section we investigate the possibility of extracting polarization fractions from VBS events without prior knowledge of the underlying dynamics. We present results both for W^+Z and for ZZ scattering. As instances of theories beyond the Standard Model (BSM), we consider a Standard Model with no Higgs boson, i.e. $M_h \to \infty$, and a Singlet extension of the Standard Model.

After the discovery of a 125 GeV mass scalar particle compatible with a Higgs boson [31, 32], the Higgsless model is not viable anymore. However, it can be considered as an extreme case of strongly coupled models: there is a large class of models whose phenomenology lies in between the SM and the Higgsless model. Deviations from the SM are expected in the large VV invariant mass region, where the vector boson longitudinal mode becomes dominant with respect to the transverse ones. The other BSM model we consider is a $\mathcal{Z}_2$ symmetric Singlet extension of the SM [33–47], which features a heavy scalar particle in addition to the (light) 125 GeV Higgs boson. The new heavy Higgs, is characterized by $M_H = 600$ GeV, $\Gamma_H = 6.45$ GeV. Its interactions are related by simple multiplicative factors to those of the light Higgs. Both sets of couplings are determined by the mixing angle α, while the ratio between the two vacuum expectation values is parametrized by an angle β. In the following, we assume $\sin \alpha = 0.2$ and $\tan \beta = 0.3$ [48–50]. In addition to the SM like couplings, the heavy Higgs couples to a light Higgs bosons pair. Deviations from the SM are expected in the VV invariant mass spectrum, around the heavy Higgs pole mass, if the scalar particle propagates in s channel. As for the light Higgs, the heavy Higgs couples mainly to the longitudinal modes of V bosons, therefore the deviations will concern especially the longitudinal polarization mode.

Polarization fractions are determined with two different methods. The first one relies on the expectation that the shapes of the decay angular distributions are not too sensitive to the underlying dynamics. If this is the case, one can fit the unpolarized distribution of a BSM model with a superposition of SM templates, as done in ref. [16]. The second exploits the similarity, in shape and normalization, of the transverse distributions across different models, which allows to extract the longitudinal component by subtracting the SM transverse contribution. Both methods give acceptable results within a few percent. The difference between the two determinations provides a rough estimate of the uncertainty in the extraction procedure.

All the results presented in this section have been obtained applying the complete set of cuts. For W^+Z, neutrino reconstruction is always understood.

7.1 Transverse polarizations

In sections 4–5 we have shown the Standard Model predictions for polarized W/Z bosons in ZZ and W^+Z scattering. In particular, we have considered left and right contributions
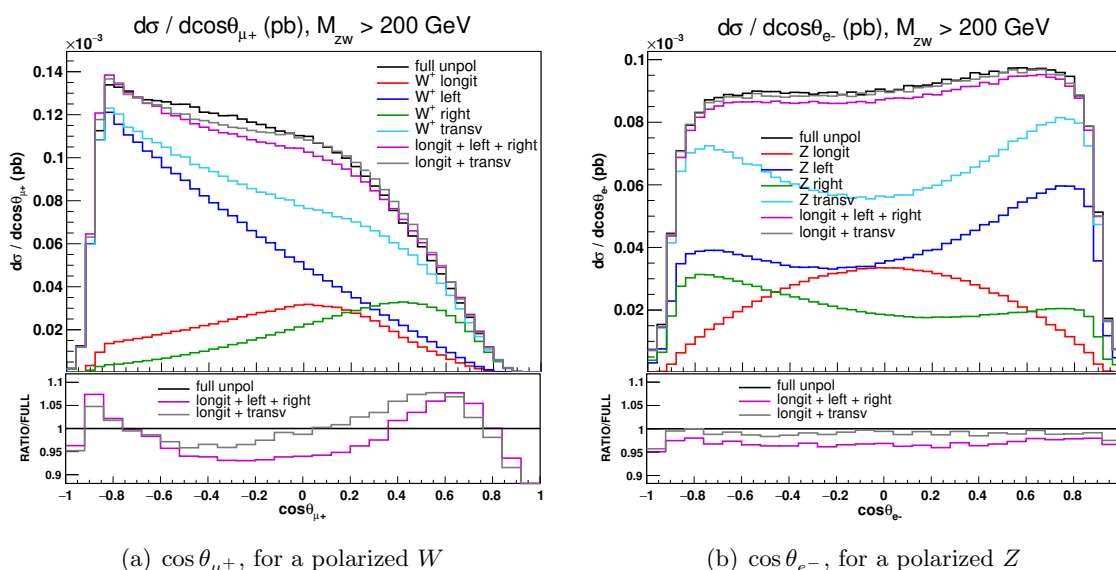
Figure 12. W^+Z scattering: comparison of transverse to left+right Standard Model distributions in $\cos\theta_{\mu^+}$ and $\cos\theta_{e^-}$ distributions, in the fiducial region ($M_{WZ} > 200$ GeV). The full set of kinematic cuts (see section 5.1) is understood.

separately. If we consider the coherent sum of left and right polarizations (which we refer to as transverse), we include the left-right interference term. Therefore, separating only the longitudinal from the transverse mode is expected to minimize the total interferences among different polarizations. That this is indeed the case can be seen in figure 12, where we show the $\cos\theta_{\mu^+}$ distributions for a polarized W^+ and the $\cos\theta_{e^-}$ distributions for a polarized Z in W^+Z scattering. If we compare the incoherent sum of left, right and longitudinal contributions (magenta curve) to the sum of transverse and longitudinal (gray curve), we find that the interferences among polarizations, defined as the difference between the full and the sum of polarized distributions, are smaller in the second case. This holds for a number of other kinematic variables. Very similar results have been obtained for a polarized Z boson in ZZ scattering. Even in the presence of BSM dynamics (either Higgsless or Singlet Extension), we reach the same conclusion. We have verified that fitting the BSM unpolarized event samples with a combination of transverse and longitudinal SM distributions gives better results than using a combination of three separate single polarized ones. Therefore, in the following we consider transverse distributions instead of left and right ones separately.

7.2 *ZZ* channel

We investigate how a different dynamics affects the longitudinal and transverse polarizations of a Z boson ($\to e^+e^-$) produced in VBS together with an unpolarized Z ($\to \mu^+\mu^-$). First, we compare the SM and the Higgsless model. Second, we compare the SM and its Singlet extension in the ZZ invariant mass window around the heavy Higgs boson pole mass.

Total cross sections [ab]				
	$M_{ZZ} > 200$ GeV		$M_{ZZ} > 500$ GeV	
Polarization	SM	NoH	SM	NoH
longitudinal	16.19(2)	27.66(3)	2.19(1)	9.72(1)
transverse	44.11(4)	46.56(5)	10.72(5)	10.95(6)
longit.+transv.	60.31(5)	74.22(6)	12.91(5)	20.67(6)
full unpolarized	61.00(6)	75.10(8)	12.87(1)	20.68(2)

Table 16. SM and Higgsless total cross sections (*ab*) for *ZZ* scattering, in the whole fiducial region and for $M_{ZZ} > 500$ GeV.

(a) M_{ZZ}

(b) $\cos\theta_{e^-}$
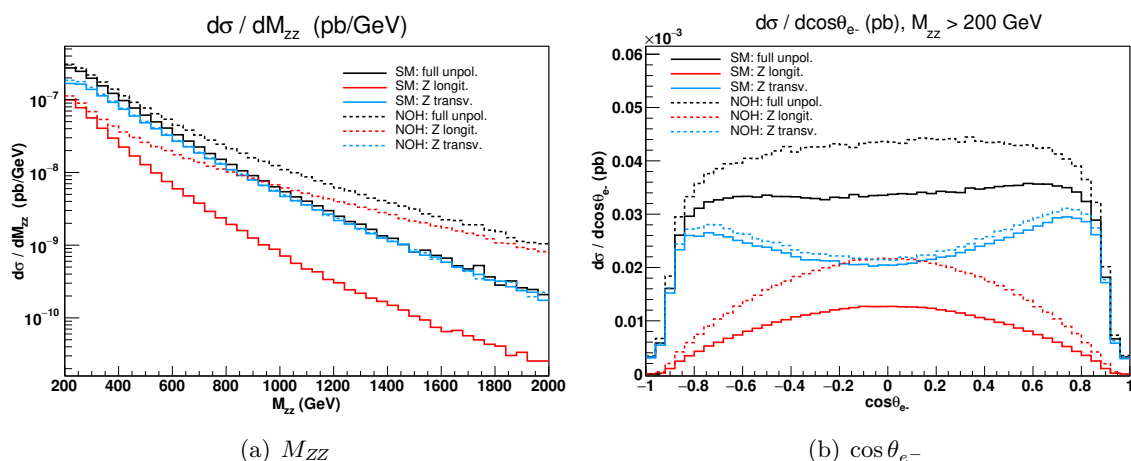
Figure 13. *ZZ* scattering: comparison of Standard Model (solid) and Higgsless model (dashed) distributions in M_{ZZ} and $\cos\theta_{e^-}$, in the fiducial region ($M_{ZZ} > 200$ GeV). The full set of kinematic cuts (see section 4.1) is understood.

The SM and Higgsless total cross sections for the polarized processes are shown in table 16, in the complete fiducial region ($M_{ZZ} > 200$ GeV) and in the large invariant mass regime ($M_{ZZ} > 500$ GeV).

The bulk of the difference between the SM and the Higgsless model is due to the longitudinal contribution, while the transverse one is only weakly sensitive to the underlying dynamics, as it has been already observed in W^+W^- scattering [16]. The Higgsless transverse component is just 4% larger than the SM one in the full fiducial volume, 2% when considering only four lepton invariant masses larger than 500 GeV. The longitudinal cross section in the Higgsless model, by contrast, is larger than the SM one by 70% in the $M_{ZZ} > 200$ GeV region and by more than a factor four for $M_{ZZ} > 500$ GeV.

These effects are even more evident in the differential cross sections shown in figure 13. The SM longitudinal M_{ZZ} distribution decreases much more rapidly than the corresponding Higgsless one at large invariant boson boson invariant mass. A very similar, though milder, effect is present also in *WZ* scattering, as it can be observed comparing figures 13(a), 17(a), and 19(a).

The similarity of Higgsless and SM transverse components can be appreciated in figure 13(b), where we present the $\cos\theta_{e^-}$ distributions for both models. Transverse distributions (azure curves) differ by an almost constant 5% factor bin by bin. However they feature the same shape. This shape similarity is true even for the longitudinal distributions (red curves), despite a huge difference in terms of total cross sections. This holds in any of the interesting kinematic regions within the fiducial volume.

Given these premises, we try to extract the polarization fractions from the Higgsless model unpolarized $\cos\theta_{e^-}$ distribution using SM templates, as done in ref. [16]. We compute the SM $\cos\theta_{e^-}$ polarized and interference normalized distributions, F_0^{SM}, $F_{\mathrm{T}}^{\mathrm{SM}}$ and $F_{\mathrm{I}}^{\mathrm{SM}}$. Then we fit the unpolarized $d\sigma_{\mathrm{full}}^{\mathrm{NoH}}/d\cos\theta_{e^-}$ distribution of the Higgsless model with a superposition of the three SM templates,

$$f(\{\mathcal{C}_\lambda\}, \cos\theta_{e^-}) = \sum_{\lambda=0,T,I} \mathcal{C}_\lambda \, F_\lambda^{\mathrm{SM}}(\cos\theta_{e^-}) \,. \tag{7.1}$$

We estimate the best parameters $\overline{\mathcal{C}}_\lambda$ by means of a simple χ^2 minimization. In order to evaluate the fit goodness we check:

1. that $f(\{\overline{\mathcal{C}}_\lambda\}, \cos\theta_{e^-})$ reproduces correctly $d\sigma_{\mathrm{full}}^{\mathrm{NoH}}/d\cos\theta_{e^-}$, and

2. that each term of the sum after minimization ($\overline{\mathcal{C}}_\lambda \, F_\lambda^{\mathrm{SM}}$) reproduces the correspondent Higgsless polarized distribution $d\sigma_\lambda^{\mathrm{NoH}}/d\cos\theta_{e^-}$.

Taking advantage of the strong similarity of the SM and Higgsless transverse differential cross sections, we have also examined an alternative procedure to extract the longitudinal component, which assumes that the transverse components and the interference are identical to the SM ones. This allows to subtract them from the full Higgsless distribution, in order to deduce the Higgsless longitudinal differential cross section. This subtraction procedure is characterized by a strong bias on the transverse and interference terms, which are assumed to be independent of the underlying dynamics, which is supposed, in other words, to have a significant effect only on the longitudinal polarization of vector bosons.

We have performed the fit and the subtraction procedure to extract the Higgsless longitudinal component in the full fiducial region and in the large M_{ZZ} region. The results are shown in figure 14. When including small values of M_{ZZ}, the difference between SM and Higgsless transverse cross sections propagates to the subtraction procedure, leading to a 9.5% overestimate of the Higgsless longitudinal cross section. When the analysis is restricted to the region $M_{ZZ} > 500\,\mathrm{GeV}$, the longitudinal component is estimated much better, with the total cross section just 2.8% larger than the expected value. When looking at even larger masses, the subtraction procedure improves again (+1.5% for $M_{ZZ} > 1000\,\mathrm{GeV}$). On the contrary, the fit procedure slightly underestimates the longitudinal component in almost all invariant mass regions. However, it works better than the subtraction approach when considering the full ZZ invariant mass range. The longitudinal contribution is estimated with at maximum 3% discrepancy with respect to the expected value. For $M_{ZZ} > 200\,\mathrm{GeV}$, the fit underestimates the longitudinal cross section by only 1.4%.
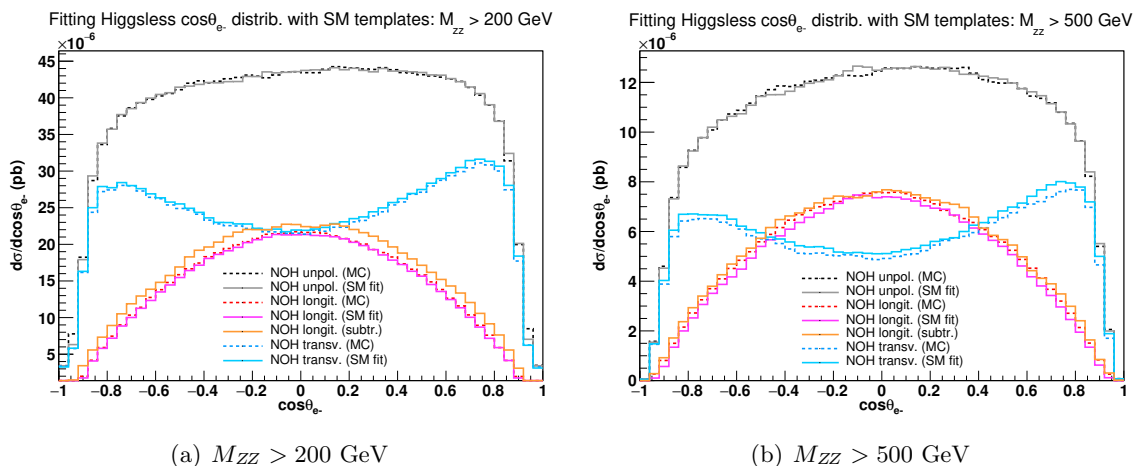
Figure 14. *ZZ* scattering: fit of the Higgsless unpolarized $\cos\theta_{e^-}$ distribution with SM templates. Fitted and expected differential cross sections in two *ZZ* invariant mass regions. For the longitudinal component the result of the fit (magenta) and the one of the subtraction technique (orange) are compared with the Monte Carlo expectations (dashed red).

These results suggest that, given the model (quasi)independence of transverse and longitudinal $\cos\theta_\ell$ shapes, a more refined fitting method should enable the extraction of polarized cross section from LHC data with satisfactory accuracy. The discrepancy in the transverse cross section between the two models, despite being small and under control, hampers an accurate extraction of the longitudinal cross section of the Higgsless model by subtracting SM distributions.

We now present a few results on the comparison between the SM and its Singlet extension in the invariant mass region of the heavy Higgs resonance. The polarized and unpolarized M_{ZZ} distributions for both models are shown in figure 15(a). The Singlet longitudinal distribution (dashed red curve) features a Breit-Wigner resonance on top of the decreasing SM distribution (solid red curve). Even the transverse component is partially affected by the additional scalar particle, as can be seen from the small bump of the dashed blue curve around 600 GeV.

The $\cos\theta_{e^-}$ distributions in the region 550 GeV $< M_{ZZ} <$ 650 GeV are shown in figure 15(b). In figure 15(c) we show the longitudinal and transverse normalized $\cos\theta_{e^-}$ shapes for the two models. The transverse component is essentially insensitive to the presence of the additional resonance, as the similarity of the blue curves demonstrates, both in shape and total cross section in the resonance region with a 2.6% discrepancy. The shape of the longitudinal component is impressively similar for the two models, despite a large difference in the total cross section. This holds even when considering a narrower invariant mass region about the heavy Higgs pole mass, e.g. 590 GeV $< M_{ZZ} <$ 610 GeV.

We have performed the fit for a ± 50 GeV and ± 10 GeV mass window around M_H. The result of the fit, shown in figure 16, underestimates by less than 4% the longitudinal cross section obtained directly with the Monte Carlo. Conversely, the transverse component is slightly overestimated. Even better results can be obtained via the subtraction procedure.
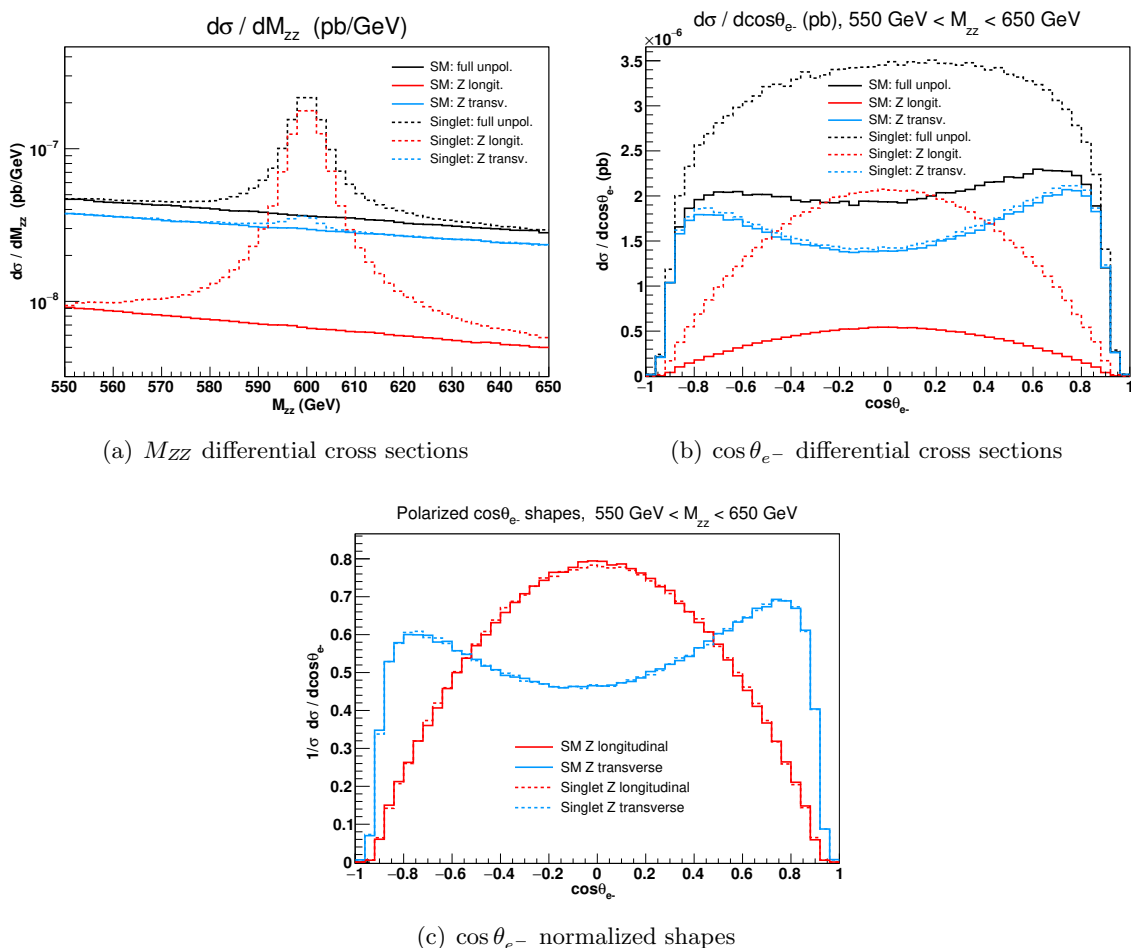
(a) M_{ZZ} differential cross sections

(b) $\cos\theta_{e^-}$ differential cross sections

(c) $\cos\theta_{e^-}$ normalized shapes

Figure 15. *ZZ* scattering: comparison of Standard Model (solid) and Singlet (dashed) distributions in M_{ZZ} and $\cos\theta_{e^-}$, in the heavy Higgs resonance region ($M_H = 600$ GeV). The full set of kinematic cuts (see section 4.1) is understood.

The longitudinal cross section in this case is reproduced with a $+2.5\%$ error. These last results give us confidence that even in the presence of additional resonances interfering with the SM, it is possible to extract the longitudinal component from LHC data with a few percent accuracy.

7.3 Polarized W in the W^+Z channel

In a similar fashion as in section 7.2, we investigate how different dynamics affect vector boson polarizations in W^+Z scattering. Since the Higgs contributes to W^+Z VBS production only in the t/u channels, an additional heavy Higgs is expected to produce a rather small enhancement of the total cross section. Therefore, we present only results for the Higgsless model.

Let's consider first a W^+ with given polarization and an unpolarized Z. The difference in the total cross section between the SM and the Higgsless model is due to the longitudinal contribution, while the transverse result is even less sensitive to the underly-
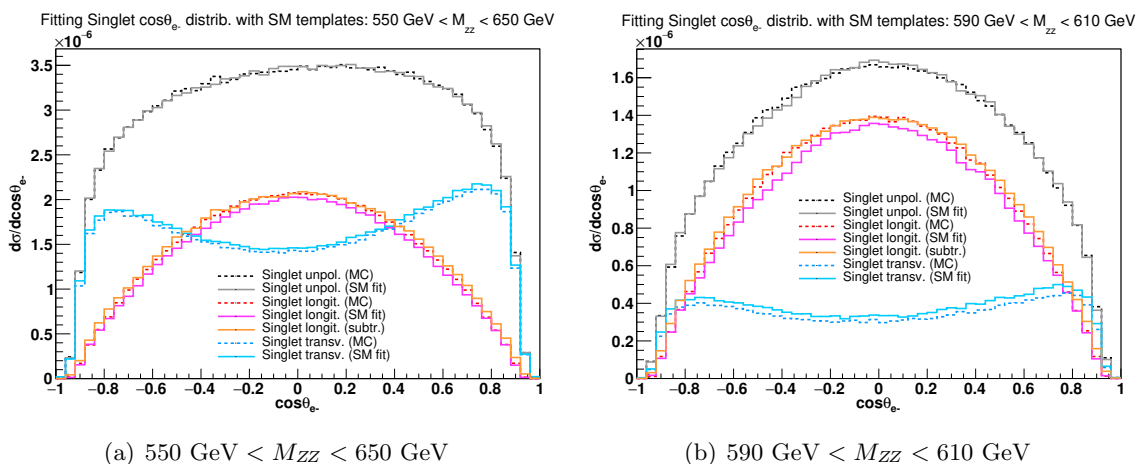
(a) $550 \text{ GeV} < M_{ZZ} < 650 \text{ GeV}$

(b) $590 \text{ GeV} < M_{ZZ} < 610 \text{ GeV}$

Figure 16. *ZZ* scattering: fit of Singlet unpolarized $\cos\theta_{e^-}$ distribution with SM templates. Fitted and expected differential cross sections in two *ZZ* invariant mass windows about the heavy Higgs pole mass. For the longitudinal component the result of the fit (magenta) and the subtraction technique one (orange) are compared with the Monte Carlo expectation (dashed red).
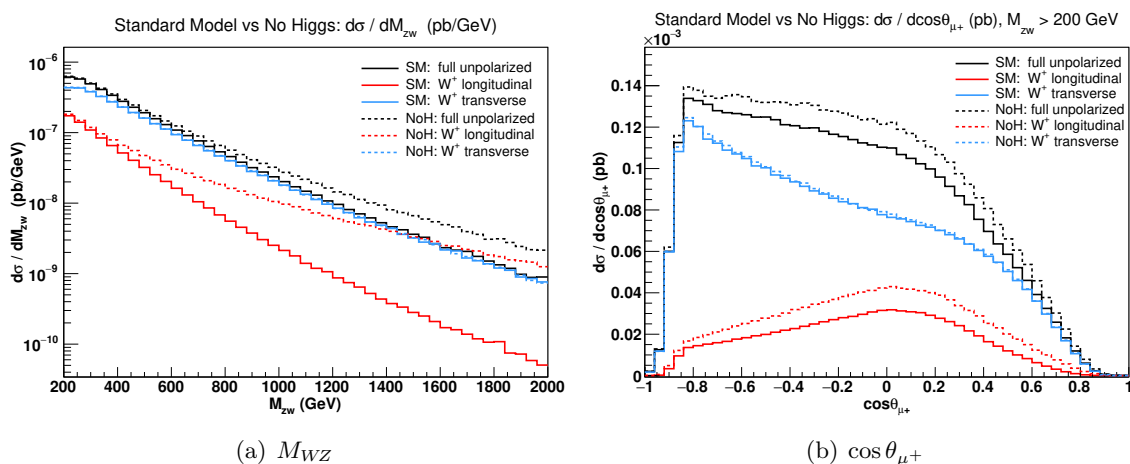

(a) M_{WZ}

(b) $\cos\theta_{\mu^+}$

Figure 17. W^+Z scattering: comparison of Standard Model (solid) and Higgsless model (dashed) distributions in M_{WZ} and $\cos\theta_{\mu^+}$. Polarized distributions concern the W^+ boson. The full set of kinematic cuts (see section 5.1) is understood, including lepton and missing transverse momentum cuts, as well as neutrino reconstruction.

ing dynamics than in *ZZ* scattering. The two transverse cross sections differ by only 1%, while the SM longitudinal cross section is 40% smaller than the Higgsless one. This is confirmed for the differential cross sections, as shown in figure 17. The M_{WZ} transverse distributions shown in figure 17(a) are almost identical for the SM and the Higgsless model over the full invariant mass range. The same holds for the $\cos\theta_{\mu^+}$ distributions, shown in figure 17(b).

In the full fiducial region, the longitudinal contribution features a similar shape in the two models, which proves to be promising for an (almost) model independent fit to extract
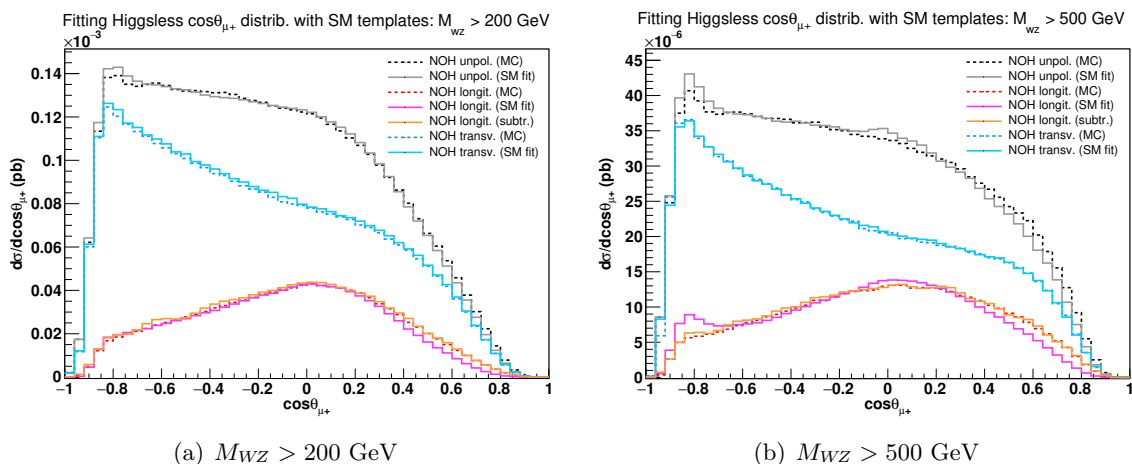
Figure 18. W^+Z scattering: fit of Higgsless unpolarized $\cos\theta_{\mu^+}$ distribution with SM templates. Fitted and expected distributions, for $M_{WZ} > 200$ GeV and $M_{WZ} > 500$ GeV.

polarization fractions from the BSM unpolarized distribution. However we will see that the similarity of longitudinal shapes is not true anymore at large M_{WZ} and large p_t^W.

As in section 7.1, using the transverse distributions rather than the left and right ones separately reduces the interferences among polarizations to 0.1% of the full unpolarized cross section. The difference between the sum of polarized distributions and the full results also decreases. Moreover, the interference shape in the two models is very similar.

As we have done for ZZ scattering, we try to extract the cross section for a polarized Z in the Higgsless model using SM polarized templates, either through a fit procedure or through direct subtraction of SM distributions. We then compare these two different predictions with the result obtained with Monte Carlo polarized amplitudes.

We have analyzed polarized contributions in a number of kinematic regions. We show in figure 18 the results for the $\cos\theta_{\mu^+}$ differential distributions, both in the whole fiducial region ($M_{WZ} > 200$ GeV) and for $M_{WZ} > 500$ GeV. In table 17 we show the numerical results of the fit and subtraction procedure for the longitudinal and transverse cross sections in each of the analyzed kinematic regions.

In the total fiducial region, the Higgsless longitudinal component is reproduced fairly well by the fit, both in total cross section (-4%) and in shape (at most 5% discrepancy, bin by bin). The transverse cross section is overestimated by 3%. Much better results are obtained with the subtraction procedure, thanks to the very small difference (approximately 1% in terms of total cross sections) between the SM and Higgsless transverse component. In this case both the total cross section (1.5% discrepancy) and the $\cos\theta_{\mu^+}$ distributions (at most 4% discrepancies, bin by bin) for the longitudinal component are reproduced accurately, as shown in figure 18(a).

When considering less inclusive regions, e.g. at large WZ invariant mass, the Higgsless and SM longitudinal $\cos\theta_{\mu^+}$ shapes start to differ, as shown in figure 18(b). This results in a poor fit in the region $M_{WZ} > 500$ GeV. However, for the cross sections, the longitudinal

	Polarized cross sections [ab]					
	Longitudinal			Transverse		
kinematic region	MC	Fit	Subtr.	MC	Fit	Subtr.
$M_{WZ} > 200$ GeV	46.90	44.93	48.37	133.10	135.16	131.73
$M_{WZ} > 500$ GeV	16.06	15.89	16.42	38.14	38.23	37.83
$M_{WZ} > 1000$ GeV	4.71	5.20	4.73	5.50	4.79	5.47
$M_{WZ} > 200$ GeV, $p_t^W > 200$ GeV	13.49	13.09	13.78	43.90	44.26	43.51
$M_{WZ} > 200$ GeV, $p_t^W > 300$ GeV	7.89	7.81	7.93	19.61	19.66	19.40
$M_{WZ} > 200$ GeV, $p_t^W > 400$ GeV	4.81	4.79	4.84	9.12	9.26	9.03
$M_{WZ} > 200$ GeV, $|\eta_W| < 1$	17.65	15.07	18.41	62.61	65.16	61.83
$M_{WZ} > 200$ GeV, $1 < |\eta_W| < 2$	19.42	19.36	19.95	55.91	55.70	55.35
$M_{WZ} > 200$ GeV, $2 < |\eta_W| < 3$	8.09	8.17	8.27	13.76	13.88	13.72
$M_{WZ} > 200$ GeV, $|\eta_W| > 3$	1.74	1.70	1.73	0.83	0.83	0.82

Table 17. Cross sections (ab), for a longitudinal and transverse W^+ in W^+Z scattering, in the Higgsless model, in several kinematic regions: comparison of MC predictions for the Higgsless model with results obtained via fit and subtraction procedure. The subtraction procedure results for a transverse W^+ coincide with the SM cross sections.

component is only 1% smaller than the Monte Carlo value. The full distributions, as well as the transverse ones, are reproduced fairly well by the fit.

When the minimum cut on M_{WZ} is pushed up to 1000 GeV, the fit reproduces the expected polarized distributions with at most 10% discrepancies, bin by bin. This shows that a model independent fit can become inaccurate in some kinematic regimes.

On the contrary, longitudinal $\cos\theta_{\mu^+}$ distributions in the Higgsless case are reproduced by the subtracted SM distributions within a few percent, in each of the kinematic regions. In the high energy and forward rapidity regions ($M_{WZ} > 1000$ GeV, $p_t^W > 400$ GeV, $|\eta_W| > 3$), which are the mostly interesting regions for new physics effects in VBS, the subtraction procedure reproduces very accurately the Monte Carlo longitudinal cross sections for the Higgsless model, since the transverse components in the two models differ by less than 1%.

The fit results presented in this section show that a model independent extraction of the W polarization fractions is problematic, due to the lack of universality of the longitudinal $\cos\theta_{\mu^+}$ shapes in this case. This is not only due to the details of neutrino reconstruction: we have checked that the fit procedure provides inaccurate results both using a different neutrino reconstruction scheme and using the true neutrino momentum. Even in these cases the longitudinal shapes are noticeably model dependent. A factor which contributes to these shape differences is the strong missing transverse momentum cut ($p_t^{\text{miss}} > 40$ GeV), which is much harder than the p_t cut on the anti muon ($p_t^\ell > 20$ GeV). This introduces a strong asymmetry when boosting into the W rest frame to compute $\cos\theta_{\mu^+}$, even without
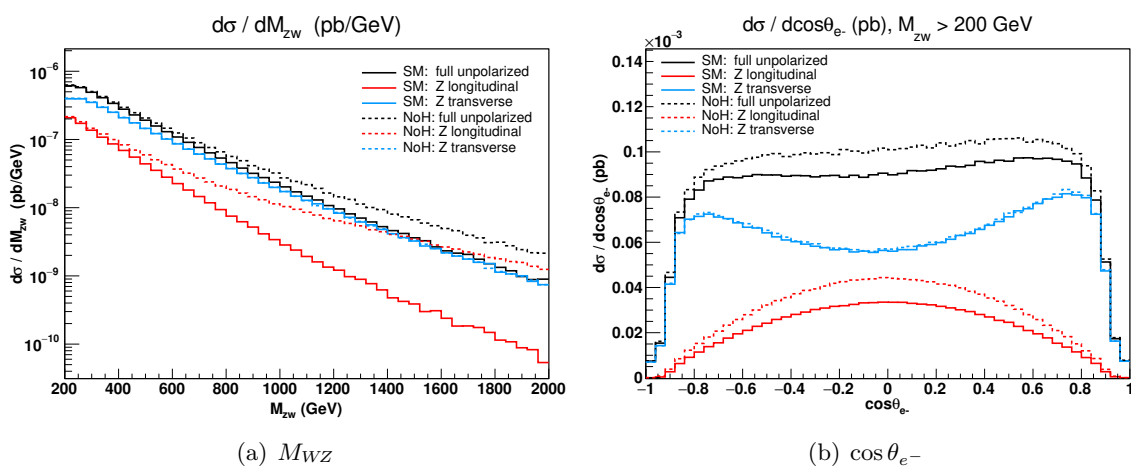
Figure 19. W^+Z scattering: comparison of Standard Model (solid) and Higgsless model (dashed) distributions in M_{WZ} and $\cos\theta_{e^-}$. Polarized distributions concern the Z boson. The full set of kinematic cuts (see section 5.1) is understood, including lepton and missing transverse momentum cuts, as well as neutrino reconstruction.

neutrino reconstruction. The differences in the p_t^{miss} distribution between the SM and the Higgsless case are larger than for the $p_t^{\mu^+}$ one and, as a consequence, have a larger effect. On the contrary, the subtraction procedure has proved promising, despite the strong assumptions it relies on. The similarity of the transverse cross sections in the SM and in the strong coupling regime is remarkable and should be investigated further, both in a general EFT framework, and assuming other specific BSM dynamics.

7.4 Polarized Z in the W^+Z channel

We now consider a polarized Z boson produced via VBS in association with an unpolarized W^+. Differently from the W, the Z boson can be entirely reconstructed. We then focus on the distributions of the cosine of the electron angle in the Z CM frame ($\cos\theta_{e^-}$).

As observed previously for the W^+, the transverse polarizations of the Z boson give the same contribution, within 1%, to the total cross section in the SM and in the Higgsless model. Furthermore, both in the SM and in the Higgsless model the adoption of the transverse component (coherent sum) allows to minimize the interferences, reproducing at the percent level the full result, when summed to the longitudinal contribution. The Higgsless longitudinal component is 30% larger than the Standard Model one.

As for the W, at large boson boson invariant mass the longitudinal component in the Higgsless model dominates. This effect can be observed in figure 19(a). The transverse differential distributions are almost identical, even at very large four lepton invariant masses.

In figure 19(b), we present the $\cos\theta_{e^-}$ distributions for a polarized Z boson. The transverse components are almost identical, both in shape and cross section. The longitudinal component features a very similar shape in the two models.

We have determined the longitudinal cross section for the Higgsless model, both through a fit and with the subtraction technique. Both procedures provide longitudinal

	Polarized cross sections [ab]					
	Longitudinal			Transverse		
kinematic region	MC	Fit	Subtr.	MC	Fit	Subtr.
$M_{WZ} > 200$ GeV	56.27	54.88	57.75	122.24	124.46	120.96
$M_{WZ} > 500$ GeV	18.35	17.59	18.63	35.46	36.30	35.26
$M_{WZ} > 1000$ GeV	4.90	4.73	4.91	5.37	5.54	5.39
$M_{WZ} > 200$ GeV, $p_t^Z > 200$ GeV	13.97	13.58	14.30	37.91	38.31	37.59
$M_{WZ} > 200$ GeV, $p_t^Z > 300$ GeV	8.16	8.13	8.29	17.05	17.11	16.93
$M_{WZ} > 200$ GeV, $p_t^Z > 400$ GeV	4.94	4.84	4.99	7.92	8.05	7.92
$M_{WZ} > 200$ GeV, $|\eta_Z| < 1$	19.22	18.32	19.99	62.76	63.69	61.95
$M_{WZ} > 200$ GeV, $1 < |\eta_Z| < 2$	22.41	22.42	23.03	45.42	45.59	45.08
$M_{WZ} > 200$ GeV, $2 < |\eta_Z| < 3$	11.72	11.51	11.76	13.31	13.72	13.22
$M_{WZ} > 200$ GeV, $|\eta_Z| > 3$	2.92	2.83	2.94	0.71	0.89	0.71

Table 18. Cross sections (ab) for a longitudinal and transverse Z in W^+Z scattering, in the Higgsless model, in several kinematic regions: comparison of MC predictions for the Higgsless model with results obtained via fit and subtraction procedure. The subtraction procedure results for a transverse Z coincide with the SM cross sections.
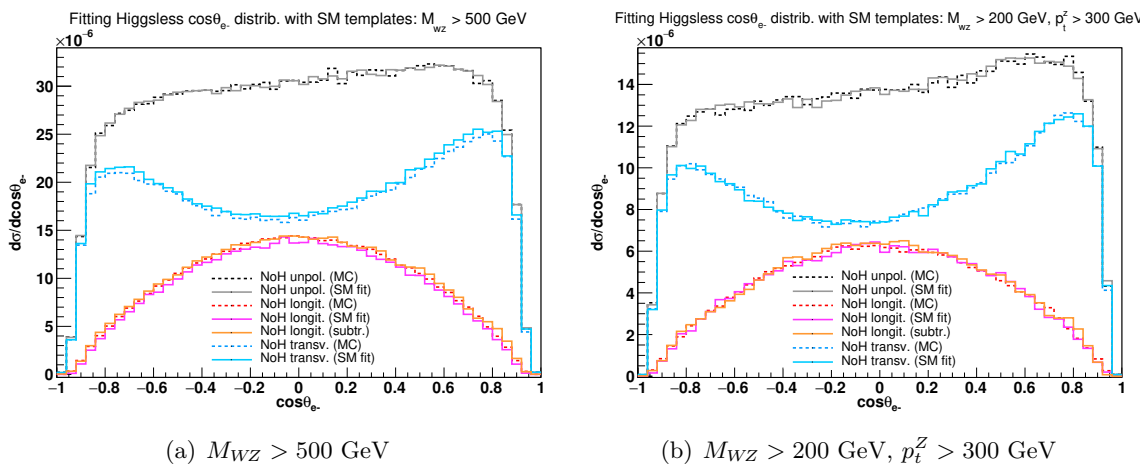

(a) $M_{WZ} > 500$ GeV (b) $M_{WZ} > 200$ GeV, $p_t^Z > 300$ GeV

Figure 20. W^+Z scattering: fit of Higgsless unpolarized $\cos\theta_{e^-}$ distributions with SM templates, in two different kinematic regions (large mass and large p_t). For the longitudinal component the result of the fit (magenta) and the one of the subtraction technique (orange) are compared with the Monte Carlo expectation (dashed red).

cross sections which differ from the Monte Carlo expectations by less than 5%, in all the studied kinematic regions. Numerical results for extracted longitudinal and transverse cross sections are shown in table 18. Fitted and expected distributions are shown in figure 20, in two specific kinematic regions.

As a general trend, the subtraction procedure overestimates by a few percent the expected values. This is due to the assumption that the transverse component in the Higgsless model coincides with the SM one. Actually, the Higgsless transverse component is slightly larger than the SM one, and this discrepancy propagates in the extraction of the longitudinal component, giving the main contribution to the few percent discrepancy with respect to the expected value.

On the contrary, the fit procedure underestimates by few percent the expected longitudinal cross section in the various kinematic regions. This results in a very mild enhancement of the transverse component (see azure and cyan curve in figure 20). Differently from the W case, the fit benefits from the strong similarity between SM and Higgsless longitudinal shapes in each of the considered kinematic regions.

As already observed for the polarizations of the W^+, in the large invariant mass ($M_{WZ} > 1000$ GeV), large p_t ($p_t^Z > 400$ GeV), and forward rapidity ($|\eta_Z| > 2$) region the subtraction procedure reproduces very well the Monte Carlo expected longitudinal cross sections, thanks to a strong similarity of transverse cross sections in the two models.

These results seem very promising, as they suggest that a model independent extraction of polarization fractions of the Z boson is viable. Very good results have been obtained in those regions which are more interesting for new physics in VBS, i.e. large invariant mass of the four-lepton system, large transverse momentum and forward rapidity of the vector bosons.

8 Conclusions

In this paper we have presented a procedure to separate polarization states of massive weak bosons in VBS processes which involve Z bosons. We have focused on pure electroweak tree level amplitudes which give contribution to W^+Z and ZZ scattering in the fully leptonic channel at the LHC. Differently from WW scattering processes, that have been investigated in a previous work [16], separating polarizations of Z bosons has proved more involved, due to γ effects in the amplitudes.

In both scattering channels, we have checked that a sufficiently tight cut on the invariant mass of charged lepton pairs around the Z pole mass is required, to allow for the separation of resonant contributions. For W bosons in WZ scattering, we propose a single On Shell projection on W resonant diagrams, to avoid unphysical cuts on the lepton-neutrino system. We have verified that the signal for a polarized Z in ZZ and WZ, as well as the signal for a polarized W in WZ, reproduce accurately the results which can be extracted from full $\cos\theta_\ell$ distributions by means of projections onto the first three Legendre polynomials, in the absence of lepton cuts. After applying a realistic set of leptonic cuts, the sum of polarized signals reproduces the full unpolarized results within a few percent. In WZ scattering, the reconstruction of the final state neutrino generates additional effects on relevant kinematic observables.

The proposed method to separate polarizations at the level of amplitudes represents a coherent theoretical tool which can be used for LHC data analyses, and is expected to provide reliable results if the underlying theory is the Standard Model. Compared

against the results of our proposal, the reweighting method, which has been widely used to determine approximate polarized signals in presence of lepton cuts, provides inaccurate predictions particularly at high diboson invariant mass.

For the extraction of polarization fractions from LHC data, we have investigated how polarized distributions change with a different realization of the EWSB, in particular in the presence of a strongly interacting Higgs sector and an additional heavy Higgs resonance.

Both the approximate independence of the polarized distribution shapes, and the remarkable similarity of the transverse component in the Standard Model, the Higgsless model, and the Singlet Extension give us confidence that it will be possible to estimate polarization fractions with reasonable accuracy by using Standard Model angular distributions, even in the presence of new physics.

Acknowledgments

A   Neutrino reconstruction

In this appendix we present several reconstruction schemes we have tried and motivate our choice of a particular procedure.

The presence of a neutrino in WZ scattering with fully leptonic decays inhibits the complete reconstruction of the final state kinematics. To avoid this difficulty, experiments often measure related, directly observable quantities, as proxies to the decay angle distribution. Examples are L_P [12], $\cos\theta_{2D}$ [13] and R_{p_T} [51], which is mostly useful for the W^+W^+ channel. Alternatively, one can attempt to reconstruct the missing component constraining the $\ell^+\nu_\ell$ system invariant mass to be equal to the W pole mass (M_W) [52, 53].

Identifying the missing transverse momentum with the transverse neutrino momentum, p_t^ν, only the component along the beam axis, p_z^ν, is unknown. The on shell condition leads to a quadratic equation in the unknown variable p_z^ν, whose two solutions are

$$p_{z\,1,2}^\nu = \frac{p_z^\ell \xi \pm \sqrt{\Delta}}{p_\ell^{t\,2}}\,, \tag{A.1}$$

where

$$\Delta = p_z^{\ell\,2}\xi^2 - p_t^{\ell\,2}\left[E^{\ell\,2}p_t^{\nu\,2} - \xi^2\right]\,, \qquad \xi = \frac{M_W^2}{2} + \mathbf{p}_t^\ell \cdot \mathbf{p}_t^\nu\,. \tag{A.2}$$

The two solutions can be either real or complex, depending on the sign of Δ. In particular, $\Delta < 0$ if the transverse mass of the $\ell^+\nu_\ell$ system ($M_t^{\ell\nu}$) is larger than M_W. In this case, we need a procedure to determine an approximate real value. If the transverse mass is smaller than M_W, then $\Delta > 0$: in this case we need a criterion to select one of the two real solutions. The two solutions have opposite sign if $\xi^2 > (E^\ell p_t^\nu)^2$, same sign otherwise.

Several criteria have been used in experimental analyses to get rid of the ambiguity in determining the unknown longitudinal momentum in processes which involve one neutrino.

We have investigated how different reconstruction schemes fare for unpolarized VBS events. The setup is the one of section 5.1, including lepton and missing p_t cuts.

We first focus on the events with positive Δ, which represent more than 80% of our VBS sample. Afterwards, we analyse two procedures for events with $\Delta < 0$.

A.1 Positive Δ

For $\Delta > 0$, we compare five different reconstruction criteria, which we describe briefly in the following.

[DeltaR] If $p^\nu_{z\,1} \cdot p^\nu_{z\,2} < 0$, choose the solution with the same sign as p^ℓ_z. Otherwise, choose the solution corresponding to the minimum $\Delta R_{\ell\nu}$. This procedure is detailed in ref. [54] and was employed for semileptonic VBS in ref. [55]. Actually, $\Delta R_{\ell\nu}$ has no discriminating power, since the two solutions give the same $\Delta\eta_{\ell\nu}$, as can be easily shown in light cone coordinates. Thus, we have decided to discard this scheme.

[CoM] If $p^\nu_{z\,1} \cdot p^\nu_{z\,2} < 0$, choose the longitudinal momentum with the same sign as p^ℓ_z. If $p^\nu_{z\,1} \cdot p^\nu_{z\,2} > 0$, choose the solution which gives the minimum partonic center of mass invariant mass (M_{CoM}), which requires softer initial state partons.

[CoMmod] Choose the solution which reconstructs the minimum M_{CoM}, independently of the sign of $p^\nu_{z\,1} \cdot p^\nu_{z\,2}$.

[CMS] Choose the solution with minimum $|p^\nu_z|$. This procedure has been employed by CMS and ATLAS collaborations for analyses of WZ production [52, 53].

[CMSbis] If $p^\nu_{z\,1} \cdot p^\nu_{z\,2} < 0$, choose the solution with the same sign as p^ℓ_z. Otherwise, choose the solution with minimum $|p^z_\nu|$.

In order to evaluate the goodness of each reconstruction scheme, we compute the distribution of the relative difference between the reconstructed and true value of the neutrino longitudinal momentum, δ_{p_z}, defined as

$$\delta_{p_z} = \frac{p_z^{\nu,\,\mathrm{reco}} - p_z^{\nu,\,\mathrm{true}}}{|p_z^{\nu,\,\mathrm{true}}|}\,.$$

We note that total final state invariant mass and the longitudinal momentum of the neutrino are strongly and positively correlated, therefore minimizing M_{CoM} (as in CoMmod) or directly $|p^\nu_z|$ (as in CMS) are roughly equivalent procedures. This results in small differences between the CoMmod and CMS distributions, as well as between the CoM and the CMSbis distributions, as shown in figure 21(a). A crucial role is played by the events with $p^\nu_{z\,1} \cdot p^\nu_{z\,2} < 0$. If we select the solution with the same sign as p^ℓ_z (CoM, CMSbis), the δ_{p_z} distribution develops a discontinuity in the region $1 < |\delta_{p_z}| < 2$, which brings the reconstructed distribution closer to the true one. Otherwise, the distributions are smooth (CoMmod, CMS).

Therefore, in addition to the relative shift in p^ν_z, we evaluate how $\cos\theta_{\mu^+}$ distributions are affected by reconstruction schemes, since this angular variable has the most relevant role
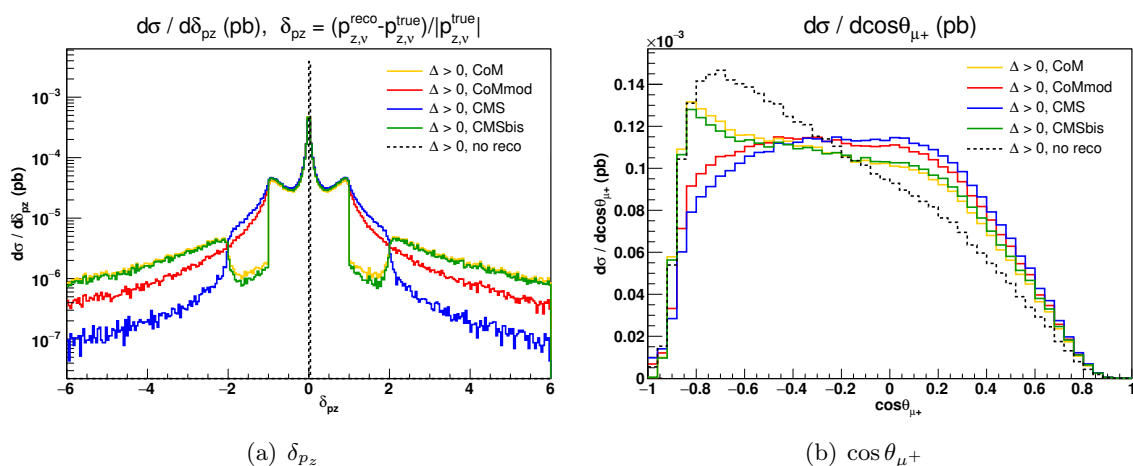
Figure 21. W^+Z scattering: neutrino reconstruction, $\Delta > 0$. Distributions in $\delta_{p_z} = (p_z^{\nu,\,\mathrm{reco}} - p_z^{\nu,\,\mathrm{true}})/|p_z^{\nu,\,\mathrm{true}}|$ and $\cos\theta_{\mu^+}$, obtained with several reconstruction procedures (solid curves), compared with the generated ones (dashed curve). The following set of cuts is understood: $p_t^j > 20\,\mathrm{GeV}$, $|\eta_j| < 5$, $M_{jj} > 500\,\mathrm{GeV}$, $\Delta\eta_{jj} > 2.5$ $p_t^\ell > 20\,\mathrm{GeV}$, $|\eta_\ell| < 2.5$, $p_t^{\mathrm{miss}} > 40\,\mathrm{GeV}$, $|M_{e^+e^-} - M_Z| < 15\,\mathrm{GeV}$.

in the phenomenology of polarized bosons. In figure 21(b) we show the reconstructed, unpolarized $\cos\theta_{\mu^+}$ distributions (solid curves), compared with the true distribution (dashed curve). The peak around -0.7 is not reproduced at all by `CMS, CoMmod` schemes. On the contrary, the other two schemes describe better the correct shape of the angular distribution over the whole range, even though not very precisely.

In this paper we have then adopted the `CoM` prescription to reconstruct events with $\Delta > 0$ since it reproduces better the $\cos\theta_\ell$ distribution.

A.2 Negative Δ

For $\Delta < 0$, we consider two options to extract a real solution from eq. (A.1).

[`poleMw`] p_z^ν is set equal to the real part of the two solutions [54]:

$$p_z^{\nu\,\mathrm{reco}} = \frac{p_\ell^z\,\xi}{p_\ell^{t\,2}} \tag{A.3}$$

[`transvMlv`] The W pole mass M_W in eqs. (A.1)–(A.2) is substituted with the transverse mass of the lepton neutrino system [52]. This forces $\Delta = 0$, and leads to:

$$p_z^{\nu\,\mathrm{reco}} = p_\ell^z\,\frac{M_t^{\ell\nu\,2} + 2\mathbf{p}_t^\ell \cdot \mathbf{p}_t^\nu}{2 p_t^{\ell\,2}} = p_z^\ell\,\frac{(2 p_t^\ell p_t^\nu - 2\mathbf{p}_t^\ell \cdot \mathbf{p}_t^\nu) + 2\mathbf{p}_t^\ell \cdot \mathbf{p}_t^\nu}{2 p_t^{\ell\,2}} = p_z^\ell\,\frac{p_t^\nu}{p_t^\ell} \tag{A.4}$$

For unpolarized VBS, it turns out that events with negative Δ account for less than 20% of the total events. The two reconstruction procedures discussed here differ by a few percent bin by bin in the δ_{p_z} distribution, both in the central peak region and in the tails. The standard deviation of the distribution suggests that the transverse mass method works slightly better, thus we have adopted it.

References

[1] CMS collaboration, *Measurement of vector boson scattering and constraints on anomalous quartic couplings from events with four leptons and two jets in proton-proton collisions at* $\sqrt{s} = 13\,TeV$, *Phys. Lett.* **B 774** (2017) 682 [arXiv:1708.02812] [InSPIRE].

[2] CMS collaboration, *Observation of electroweak production of same-sign W boson pairs in the two jet and two same-sign lepton final state in proton-proton collisions at* $\sqrt{s} = 13\,TeV$, *Phys. Rev. Lett.* **120** (2018) 081801 [arXiv:1709.05822] [InSPIRE].

[3] ATLAS collaboration, *Observation of electroweak production of a same-sign W boson pair in association with two jets in pp collisions at* $\sqrt{s} = 13\,TeV$ *with the ATLAS detector*, arXiv:1906.03203 [InSPIRE].

[4] ATLAS collaboration, *Observation of electroweak* $W^{\pm}Z$ *boson pair production in association with two jets in pp collisions at* $\sqrt{s} = 13\,TeV$ *with the ATLAS detector*, *Phys. Lett.* **B 793** (2019) 469 [arXiv:1812.09740] [InSPIRE].

[5] CMS collaboration, *Measurement of electroweak WZ boson production and search for new physics in WZ + two jets events in pp collisions at* $\sqrt{s} = 13\,TeV$, *Phys. Lett.* **B 795** (2019) 281 [arXiv:1901.04060] [InSPIRE].

[6] CMS collaboration, *Vector Boson Scattering prospective studies in the ZZ fully leptonic decay channel for the High-Luminosity and High-Energy LHC upgrades*, CMS-PAS-FTR-18-014 [InSPIRE].

[7] HL-LHC and HE-LHC Working Group collaborations, *Standard Model Physics at the HL-LHC and HE-LHC*, arXiv:1902.04070 [InSPIRE].

[8] Z. Bern et al., *Left-Handed W Bosons at the LHC*, *Phys. Rev.* **D 84** (2011) 034008 [arXiv:1103.5445] [InSPIRE].

[9] W.J. Stirling and E. Vryonidou, *Electroweak gauge boson polarisation at the LHC*, *JHEP* **07** (2012) 124 [arXiv:1204.6427] [InSPIRE].

[10] A. Belyaev and D. Ross, *What Does the CMS Measurement of W-polarization Tell Us about the Underlying Theory of the Coupling of W-Bosons to Matter?*, *JHEP* **08** (2013) 120 [arXiv:1303.3297] [InSPIRE].

[11] J. Baglio and N. Le Duc, *Fiducial polarization observables in hadronic WZ production: A next-to-leading order QCD+EW study*, *JHEP* **04** (2019) 065 [arXiv:1810.11034] [InSPIRE].

[12] CMS collaboration, *Measurement of the Polarization of W Bosons with Large Transverse Momenta in W+Jets Events at the LHC*, *Phys. Rev. Lett.* **107** (2011) 021802 [arXiv:1104.3829] [InSPIRE].

[13] ATLAS collaboration, *Measurement of the polarisation of W bosons produced with large transverse momentum in pp collisions at* $\sqrt{s} = 7\,TeV$ *with the ATLAS experiment*, *Eur. Phys. J.* **C 72** (2012) 2001 [arXiv:1203.2165] [InSPIRE].

[14] ATLAS collaboration, *Measurement of the W boson polarisation in $t\bar{t}$ events from pp collisions at $\sqrt{s} = 8\,TeV$ in the lepton + jets channel with ATLAS*, *Eur. Phys. J.* **C 77** (2017) 264 [*Erratum ibid.* **C 79** (2019) 19] [arXiv:1612.02577] [INSPIRE].

[15] CMS collaboration, *Measurement of the W boson helicity fractions in the decays of top quark pairs to lepton + jets final states produced in pp collisions at $\sqrt{s} = 8\,TeV$*, *Phys. Lett.* **B 762** (2016) 512 [arXiv:1605.09047] [INSPIRE].

[16] A. Ballestrero, E. Maina and G. Pelliccioli, *W boson polarization in vector boson scattering at the LHC*, *JHEP* **03** (2018) 170 [arXiv:1710.09339] [INSPIRE].

[17] A. Kadeer, J.G. Körner and U. Moosbrugger, *Helicity analysis of semileptonic hyperon decays including lepton mass effects*, *Eur. Phys. J.* **C 59** (2009) 27 [hep-ph/0511019] [INSPIRE].

[18] A. Aeppli, F. Cuypers and G.J. van Oldenborgh, *O(Γ) corrections to W pair production in e^+e^- and γγ collisions*, *Phys. Lett.* **B 314** (1993) 413 [hep-ph/9303236] [INSPIRE].

[19] A. Aeppli, G.J. van Oldenborgh and D. Wyler, *Unstable particles in one loop calculations*, *Nucl. Phys.* **B 428** (1994) 126 [hep-ph/9312212] [INSPIRE].

[20] A. Denner, S. Dittmaier, M. Roth and D. Wackeroth, *Electroweak radiative corrections to $e^+e^- \to WW \to 4$ fermions in double pole approximation: The RACOONWW approach*, *Nucl. Phys.* **B 587** (2000) 67 [hep-ph/0006307] [INSPIRE].

[21] M. Billóni, S. Dittmaier, B. Jäger and C. Speckner, *Next-to-leading order electroweak corrections to $pp \to W^+W^- \to 4$ leptons at the LHC in double-pole approximation*, *JHEP* **12** (2013) 043 [arXiv:1310.1564] [INSPIRE].

[22] B. Biedermann et al., *Next-to-leading-order electroweak corrections to $pp \to W^+W^- \to 4$ leptons at the LHC*, *JHEP* **06** (2016) 065 [arXiv:1605.03419] [INSPIRE].

[23] A. Ballestrero, A. Belhouari, G. Bevilacqua, V. Kashkan and E. Maina, *PHANTOM: A Monte Carlo event generator for six parton final states at high energy colliders*, *Comput. Phys. Commun.* **180** (2009) 401 [arXiv:0801.3359] [INSPIRE].

[24] A. Ballestrero and E. Maina, *A new method for helicity calculations*, *Phys. Lett.* **B 350** (1995) 225 [hep-ph/9403244] [INSPIRE].

[25] LHC HIGGS CROSS SECTION WORKING GROUP collaboration, *Handbook of LHC Higgs Cross Sections: 4. Deciphering the Nature of the Higgs Sector*, arXiv:1610.07922 [INSPIRE].

[26] A. Denner, S. Dittmaier, P. Maierhöfer, M. Pellen and C. Schwan, *QCD and electroweak corrections to WZ scattering at the LHC*, *JHEP* **06** (2019) 067 [arXiv:1904.00882] [INSPIRE].

[27] B. Jäger, A. Karlberg and J. Scheller, *Parton-shower effects in electroweak $WZjj$ production at the next-to-leading order of QCD*, *Eur. Phys. J.* **C 79** (2019) 226 [arXiv:1812.05118] [INSPIRE].

[28] C. Bittrich, *Study of Polarization Fractions in the Scattering of Massive Gauge Bosons $W^{\pm}Z \to W^{\pm}Z$ with the ATLAS Detector at the Large Hadron Collider*, MSc Thesis, Dresden, Tech. U., (2015).

[29] CMS collaboration, *Angular coefficients of Z bosons produced in pp collisions at $\sqrt{s} = 8\,TeV$ and decaying to $\mu^+\mu^-$ as a function of transverse momentum and rapidity*, *Phys. Lett.* **B 750** (2015) 154 [arXiv:1504.03512] [INSPIRE].

[30] ATLAS collaboration, *Measurement of Top Quark Polarization in Top-Antitop Events from Proton-Proton Collisions at $\sqrt{s} = 7\,TeV$ Using the ATLAS Detector*, *Phys. Rev. Lett.* **111** (2013) 232002 [arXiv:1307.6511] [INSPIRE].

[31] CMS collaboration, *Observation of a new boson at a mass of 125 GeV with the CMS experiment at the LHC*, *Phys. Lett.* **B 716** (2012) 30 [arXiv:1207.7235] [INSPIRE].

[32] ATLAS collaboration, *Observation of a new particle in the search for the Standard Model Higgs boson with the ATLAS detector at the LHC*, *Phys. Lett.* **B 716** (2012) 1 [arXiv:1207.7214] [INSPIRE].

[33] V. Silveira and A. Zee, *Scalar Phantoms*, *Phys. Lett.* **161B** (1985) 136 [INSPIRE].

[34] R.M. Schabinger and J.D. Wells, *A minimal spontaneously broken hidden sector and its impact on Higgs boson physics at the large hadron collider*, *Phys. Rev.* **D 72** (2005) 093007 [hep-ph/0509209] [INSPIRE].

[35] D. O'Connell, M.J. Ramsey-Musolf and M.B. Wise, *Minimal Extension of the Standard Model Scalar Sector*, *Phys. Rev.* **D 75** (2007) 037701 [hep-ph/0611014] [INSPIRE].

[36] O. Bahat-Treidel, Y. Grossman and Y. Rozen, *Hiding the Higgs at the LHC*, *JHEP* **05** (2007) 022 [hep-ph/0611162] [INSPIRE].

[37] V. Barger, P. Langacker, M. McCaskey, M.J. Ramsey-Musolf and G. Shaughnessy, *LHC Phenomenology of an Extended Standard Model with a Real Scalar Singlet*, *Phys. Rev.* **D 77** (2008) 035005 [arXiv:0706.4311] [INSPIRE].

[38] G. Bhattacharyya, G.C. Branco and S. Nandi, *Universal Doublet-Singlet Higgs Couplings and phenomenology at the CERN Large Hadron Collider*, *Phys. Rev.* **D 77** (2008) 117701 [arXiv:0712.2693] [INSPIRE].

[39] M. Gonderinger, Y. Li, H. Patel and M.J. Ramsey-Musolf, *Vacuum Stability, Perturbativity, and Scalar Singlet Dark Matter*, *JHEP* **01** (2010) 053 [arXiv:0910.3167] [INSPIRE].

[40] S. Dawson and W. Yan, *Hiding the Higgs Boson with Multiple Scalars*, *Phys. Rev.* **D 79** (2009) 095002 [arXiv:0904.2005] [INSPIRE].

[41] S. Bock, R. Lafaye, T. Plehn, M. Rauch, D. Zerwas and P.M. Zerwas, *Measuring Hidden Higgs and Strongly-Interacting Higgs Scenarios*, *Phys. Lett.* **B 694** (2011) 44 [arXiv:1007.2645] [INSPIRE].

[42] P.J. Fox, D. Tucker-Smith and N. Weiner, *Higgs friends and counterfeits at hadron colliders*, *JHEP* **06** (2011) 127 [arXiv:1104.5450] [INSPIRE].

[43] C. Englert, T. Plehn, D. Zerwas and P.M. Zerwas, *Exploring the Higgs portal*, *Phys. Lett.* **B 703** (2011) 298 [arXiv:1106.3097] [INSPIRE].

[44] C. Englert, J. Jaeckel, E. Re and M. Spannowsky, *Evasive Higgs Maneuvers at the LHC*, *Phys. Rev.* **D 85** (2012) 035008 [arXiv:1111.1719] [INSPIRE].

[45] B. Batell, S. Gori and L.-T. Wang, *Exploring the Higgs Portal with 10/fb at the LHC*, *JHEP* **06** (2012) 172 [arXiv:1112.5180] [INSPIRE].

[46] C. Englert, T. Plehn, M. Rauch, D. Zerwas and P.M. Zerwas, *LHC: Standard Higgs and Hidden Higgs*, *Phys. Lett.* **B 707** (2012) 512 [arXiv:1112.3007] [INSPIRE].

[47] R.S. Gupta and J.D. Wells, *Higgs boson search significance deformations due to mixed-in scalars*, *Phys. Lett.* **B 710** (2012) 154 [arXiv:1110.0824] [INSPIRE].

[48] G.M. Pruna and T. Robens, *The Higgs Singlet extension parameter space in the light of the LHC discovery*, *Phys. Rev.* **D 88** (2013) 115012 [arXiv:1303.1150] [INSPIRE].

[49] D. López-Val and T. Robens, Δr *and the W-boson mass in the singlet extension of the standard model*, *Phys. Rev.* **D 90** (2014) 114018 [arXiv:1406.1043] [INSPIRE].

[50] T. Robens and T. Stefaniak, *Status of the Higgs Singlet Extension of the Standard Model after LHC Run 1*, *Eur. Phys. J.* **C 75** (2015) 104 [arXiv:1501.02234] [INSPIRE].

[51] K. Doroba et al., *The $W_L W_L$ Scattering at the LHC: Improving the Selection Criteria*, *Phys. Rev.* **D 86** (2012) 036011 [arXiv:1201.2768] [INSPIRE].

[52] CMS collaboration, *Search for a W' or Techni-ρ Decaying into WZ in pp Collisions at $\sqrt{s} = 7\,TeV$*, *Phys. Rev. Lett.* **109** (2012) 141801 [arXiv:1206.0433] [INSPIRE].

[53] ATLAS collaboration, *Measurement of $W^{\pm}Z$ production cross sections and gauge boson polarisation in pp collisions at $\sqrt{s} = 13\,TeV$ with the ATLAS detector*, *Eur. Phys. J.* **C 79** (2019) 535 [arXiv:1902.05759] [INSPIRE].

[54] CMS collaboration, CMS Note AN-2007/05.

[55] A. Ballestrero, G. Bevilacqua and E. Maina, *A complete parton level analysis of boson-boson scattering and ElectroWeak Symmetry Breaking in $\ell\nu$ + four jets production at the LHC*, *JHEP* **05** (2009) 015 [arXiv:0812.5084] [INSPIRE].